Article

Not peer-reviewed version

Design, Multiphysics Modeling and Experimental Characterization of RF AlScN Magnetoelectric Antennas

Nicol Maietta [*,†] , Samuel Quaresima [†] , Yisi Liu , Onurcan Kaya , Junhao Dong , Mingzhong Wu ,
Xufeng Zhang , Cristian Cassella

Posted Date: 11 May 2026

doi: 10.20944/preprints202605.0722.v1

Keywords: bulk acoustic wave technology; magnetoelectric antennas; aluminum scandium nitride

doi:10.20944/preprints202605.0722.v1

Article

Design, Multiphysics Modeling and Experimental Characterization of RF AlScN Magnetoelectric Antennas

Nicol Maietta [1,*,†], Samuel Quaresima [1,†], Yisi Liu [1], Onurcan Kaya [1], Junhao Dong [1], Mingzhong Wu [2], Xufeng Zhang [1] and Cristian Cassella [1]

[1] Institute for NanoSystems Innovation (NanoSI), Northeastern University, Boston, MA 02115, USA
[2] Department of Physics and Department of Electrical & Computer Engineering, Northeastern University, Boston, MA 02115, USA
[*] Correspondence: maietta.n@northeastern.edu
[†] These authors contributed equally to this work.

Abstract

Over the past decade, acoustically-actuated magnetoelectric (ME) antennas have been proposed as chip-scale radiofrequency (RF) antennas compatible with post-Complementary Metal Oxide Semiconductor (CMOS) fabrication processes. These devices have been reported to exhibit antenna gains far exceeding those of conventional electromagnetic (EM) antennas with comparable footprint. However, recent studies have challenged whether this enhanced gain originates from magnetoelastic coupling or from stray radiation sources, like the electric dipole moment in the piezoelectric film or currents in the probing pads. We resolve this controversy through a combined analytical, numerical, and experimental investigation. We model and quantify the radiated power and corresponding gain contributions from (I) magnetoelastic coupling; (II) the strain-driven, time-varying electric dipole moment in the piezoelectric layer; and (III) the currents in the probing pads. Our results confirm that the radiation from magnetoelastic coupling exceeds that of the other sources by several orders of magnitude. In addition, we explain how to optimize the return loss and the radiated power of ME antennas when connected to a 50 Ω source, showing that the optimal operating point is the anti-resonance frequency. Based on this finding, we investigate the impact of the electromechanical coupling (k_t^2) on gain and -10 dB fractional bandwidth. To corroborate our simulation results, we design, fabricate, and characterize the first two Aluminum Scandium Nitride (AlScN) magnetoelectric Bulk Acoustic Wave (BAW) antennas operating beyond 1.1 GHz. The two prototypes integrate different magnetostrictive materials (FeGaB and FeCoSiB) and exhibit measured realized gains of -31.8 dB and -29.7 dB, with -10 dB fractional bandwidths of 1.28% and 1.27% at 2.62 and 3.08 GHz, respectively. The achieved bandwidths are the highest reported for radiofrequency (RF) ME antennas, owing primarily to the enhanced piezoelectric coefficients of the AlScN. Benchmarking against control structures (unreleased FeGaB and FeCoSiB devices) confirms substantially degraded radiation performance in the absence of a strong magnetoelastic coupling. These results elucidate the working principle of ME antennas and provide RF designers with a rigorous framework for the design and modeling of acoustically actuated ME antennas for wireless communication and sensing.

Keywords: bulk acoustic wave technology; magnetoelectric antennas; aluminum scandium nitride

---

1. Introduction

Chip-scale piezoelectric Bulk Acoustic Wave (BAW) resonators have matured and become ubiquitous across radiofrequency (RF) chains. Aluminum Nitride (AlN) and Aluminum Scandium Nitride (AlScN) BAW resonators, in particular, have become popular due to their high electromechanical coupling coefficient (k_t^2) and their compatibility with Complementary Metal Oxide Semiconductor

(CMOS) fabrication processes [1–3]. BAW devices form the core of RF filters in commercial front-ends [4] and have recently enabled quartz-less frequency synthesizers for both wireless and wired communications [5]. In addition, they have been used as chip-scale high-sensitivity sensors for a variety of parameters, such as acceleration, temperature, and infrared light [6–8].

More recently, several experimental studies have suggested that AlN/AlScN BAW resonators enable chip-scale antennas with gain levels that cannot be achieved with conventional electromagnetic (EM) antennas of similar footprint [9–11], since the dimensions of the latter typically scale with the EM wavelength [12–14]. This discovery has opened exciting possibilities toward fully-integrated wireless sensor nodes for Internet-of-Things (IoT) applications. In many of the AlN/AlScN devices developed for this purpose, a magnetostrictive (MS) layer is embedded in the resonator body, and the reported high gain is attributed to magnetoelastic coupling producing strain-mediated spatiotemporal modulation of the magnetization in the MS layer [9]. However, this explanation has recently been called into question. In [15], the authors compare the performance of a BAW magnetoelectric (ME) antenna with that of a similar control device where the magnetostrictive material is replaced by an aluminum film. When employed as a transmitting antenna, the BAW ME antenna in [15] showed a minor boost in the voltage at the receiving horn antenna of merely 0.60 dB compared to the non-magnetic control device. The bulk of the radiation was thus attributed mainly to the electric dipole moment in the piezoelectric layer of the resonator. Similarly, in [16], two devices are compared: a BAW ME antenna employing Nickel (Ni) as the magnetostrictive layer, and a control device where Ni is replaced with Permalloy, a magnetic material that shows a much weaker magnetoelastic coupling. The intrinsic gain of the two devices differed by ~ 2 dB, suggesting that the main source of radiation might not be entirely magnetoelastic in nature. Finally, a new class of acoustically mediated piezoelectric (AMP) antennas have recently been reported, exhibiting large gains without leveraging magnetostrictive layers to radiate. Among them, asymmetrically excited Surface Acoustic Wave (SAW) and BAW AMP antennas [11,17] recently showed gain values comparable to those reported for prior ME counterparts.

To resolve the controversy surrounding the radiation from ME BAW antennas, we modeled, designed, fabricated, and experimentally characterized two $Al_{0.7}Sc_{0.3}N$ (hereafter simply referred to as AlScN) Film Bulk Acoustic-wave Resonator (FBAR, [18]) antennas operating at 2.6 GHz and 3.1 GHz, each incorporating a different 500 nm-thick laminated MS layer (FeGaB or FeCoSiB, both known for their large magnetostrictive coefficients [19]). To the best of our knowledge, these are the first reported AlScN BAW antennas with a 30% Sc-doping, and operating above 1.1 GHz [10]. When driven at their parallel resonance frequency (f_p), these devices achieve measured realized gains of -31.8 dB and -29.7 dB, and -10 dB fractional bandwidths of 1.28% and 1.27%, respectively. As will be highlighted in the following sections, this operating point is a key design choice because it maximizes the antennas' effective aperture, while simultaneously enabling 50 Ω-matching despite the relatively high dielectric permittivity ($\epsilon_r = 14.1$) of highly-doped AlScN films [20,21]. Using numerical and analytical models, we show that the dominant radiation mechanism is indeed magnetoelastic coupling. Specifically, we find that the power radiated by the equivalent magnetic currents and by the electric currents flowing through the probing pads is several orders of magnitude lower than the power radiated through magnetoelastic coupling. From an application perspective, our results pave the way for future wireless sensor tags using AlScN antennas rather than the much larger printed-circuit-board (PCB) antennas employed today. This approach supports scalable manufacturing (hence lower cost) and enables new classes of wireless sensor nodes with extreme degrees of miniaturization.

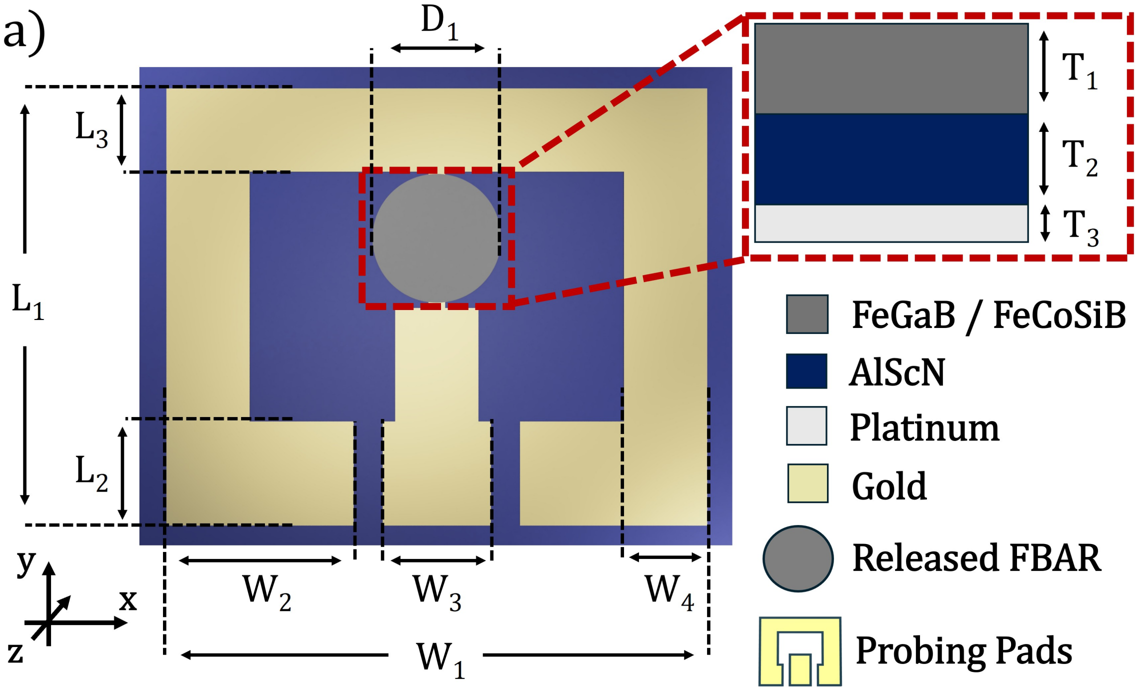

b)

[μm]	L_1	L_2	L_3	W_1	W_2	W_3	W_4	D_1	T_1	T_2	T_3
	700	200	100	800	275	150	100	200	0.5	0.5	0.08

Figure 1. a) Model of the proposed bulk acoustic wave (BAW) magnetoelectric (ME) antenna. The inset reports the cross section of the film bulk acoustic resonator (FBAR)'s released area, which incorporates the MS layer. b) In-plane and cross-sectional dimensions of the antenna.

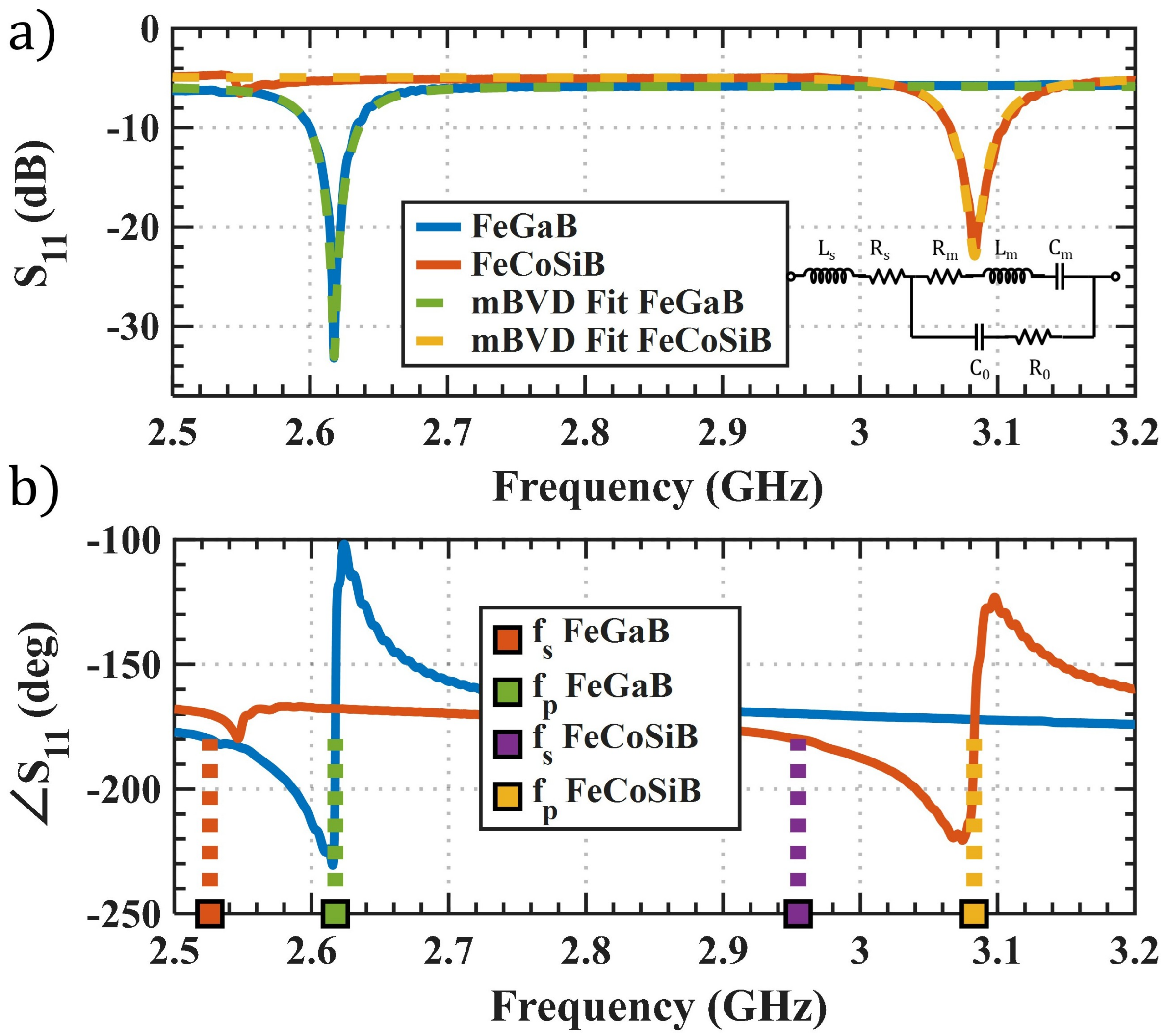

Figure 2. a) Experimentally measured and fitted magnitude of the S_{11} parameters for the FeGaB and FeCoSiB-based BAW ME antennas, which we used to extract the loss terms incorporated into the FEM simulations. The insets report a schematic of the Modified Butterworth-Van Dyke (MBVD) model. b) Experimentally measured unwrapped phase of the S_{11} parameters, where we showcase the respective series (f_s) and parallel (f_p) resonance frequencies for both devices.

2. Principle of Operation

The antennas reported in this work comprise two parts: (I) an unreleased probing pad structure and (II) a released FBAR incorporating the MS layer. The probing pads are formed by a 150 nm-thick Au layer and enable electrical characterization using ground-signal-ground (GSG) probes, while the released FBAR section is where the mechanical resonance is actuated. The FBAR stack comprises an 80 nm-thick Pt electrode, a 500 nm-thick AlScN layer, and a 500 nm-thick MS layer. In both antennas, the MS film is deposited as a laminate to mitigate eddy-current losses. A schematic of the complete structure is shown in Figure 1a, while the in-plane and out-of plane dimensions of the devices are reported in Figure 1b. We also report the measured magnitude of the experimental S_{11} parameters of both fabricated antennas in Figure 2a, together with their Modified Butterworth-Van Dyke (MBVD) equivalent circuit [22,23]. Figure 2b shows the unwrapped phase of the measured S_{11} parameters.

When electrically driven at either their series (f_s) or parallel (f_p) resonance frequencies, the two antennas excite an S_1 Lamb mode via the AlScN d_{33} piezoelectric coefficient [24]. This mode matches closely a pure thickness-extensional (TE) mode[3,25]. In practice, f_s and f_p correspond to the frequencies at which the antennas' S_{11}-trends become purely real. We also note that, for both devices, the minimum value of $|S_{11}|$ occurs at f_p, which we found to be a key design strategy to enhance the gain of ME antennas, as will be explained in Section III-d.

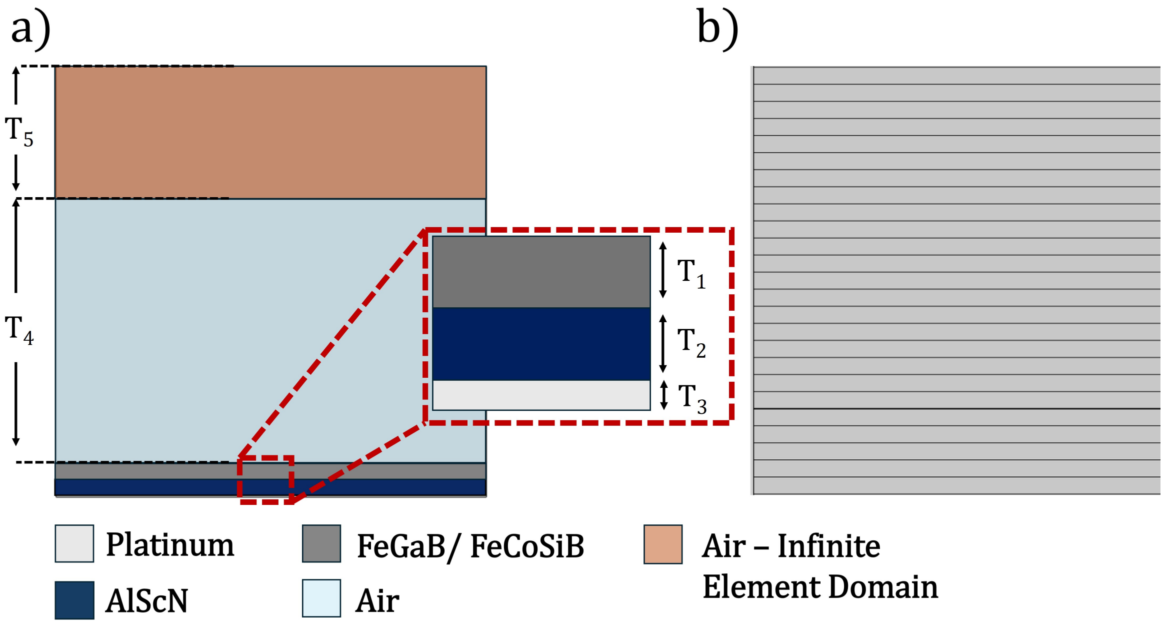

Figure 4. a) Schematics of the 2D simulation geometry considered in this work. The thickness values T used in the model are the same listed in Fig 1. b) Illustration of a portion of the mesh used in the simulations, containing 286 uniformly spaced rectangular elements. Only one element along the width direction is used due to the assumption of a purely TE mode (uniform displacement along the lateral (x) direction).

We identify three main radiation sources for the reported ME antennas, illustrated graphically in Figure 3: (I) radiation from the strain-driven time-varying magnetic dipole moment of the MS layer (magnetoelastic contribution); (II) radiation from equivalent magnetic currents along the sides of the FBAR; (III) radiation from electric currents in the probing pads [15]. In the following sections, we discuss how to compute and quantify the radiated power and the corresponding intrinsic gain contribution for each mechanism, using analytical methods or finite element methods (FEM).

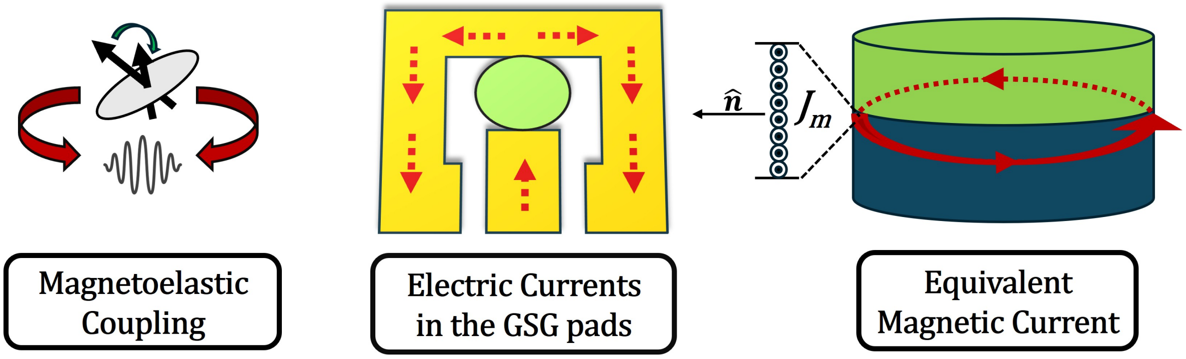

Figure 3. Illustration of the main radiation sources of BAW ME antennas.

2.1. Radiation from magnetoelastic coupling

To quantify the radiated power associated with magnetoelastic coupling, $P_{\text{rad}}^{\text{ME}}$ and the corresponding intrinsic gain contribution, G_{ME}, we employ two methodologies (“Method 1” and “Method 2”) within the same FEM simulation framework. In the following, we will first describe the FEM framework and then present the two methods, showing that they yield equivalent G_{ME} vs. frequency trends.

FEM Simulation Framework

To model our AlScN-based BAW ME antennas, we employ a coupled solid-mechanics/electromagnetics

Preprints.org (www.preprints.org) | NOT PEER-REVIEWED | Posted: 11 May 2026 doi:10.20944/preprints202605.0722.v1

FEM model, capturing the conversion of strain into AC magnetization and its associated electromagnetic fields. Since the device is electrically small over the frequency range of interest [26], we adopt a quasi-static approximation: displacement currents are neglected and the fields in and near the structure are computed from the low-frequency Maxwell equations:

$$\begin{cases} \nabla \cdot \mathbf{D} = 0, \\ \nabla \times \mathbf{H} = \mathbf{J} = \sigma \mathbf{E}. \end{cases} \tag{1}$$

These equations are then paired with the conservation of linear momentum for a continuum, relating stress $\mathbf{S}$ and displacement $\mathbf{u}$:

$$\nabla \cdot \mathbf{S} = -\rho \omega^2 \mathbf{u}, \tag{2}$$

where ρ is the mass density and ω is the angular frequency.

The system of equations is completed by the piezoelectric and piezomagnetic constitutive relations [27–29]:

$$\begin{cases} \boldsymbol{\varepsilon} = \mathbf{s}_E \mathbf{S} + \mathbf{d}^T \mathbf{E}, \\ \mathbf{D} = \mathbf{d}\mathbf{S} + \epsilon_0 \boldsymbol{\epsilon}_{rT} \mathbf{E}, \end{cases} \qquad \begin{cases} \boldsymbol{\varepsilon} = \mathbf{s}_H \mathbf{S} + \mathbf{d}_{HT}^T \mathbf{H}, \\ \mathbf{B} = \mathbf{d}_{HT} \mathbf{S} + \mu_0 \boldsymbol{\mu}_{rT} \mathbf{H}. \end{cases} \tag{3}$$

The first two relations apply to the piezoelectric layer, whereas the latter two describe the magnetoelastic response of the MS layer. Here, $\mathbf{E}$, $\mathbf{D}$, $\mathbf{H}$, and $\mathbf{B}$ are the electric field, electric displacement, magnetic field, and magnetic flux density, respectively; $\mathbf{J}$ is the free current density, σ is the electrical conductivity; $\boldsymbol{\varepsilon}$ is the strain tensor; $\mathbf{s}_E$ and $\mathbf{s}_H$ are the compliance matrices at constant electric and magnetic field, respectively; $\mathbf{d}$ and $\mathbf{d}_{HT}$ are the piezoelectric and piezomagnetic coupling matrices; ϵ_0 and μ_0 are the permittivity and permeability of free space; $\boldsymbol{\epsilon}_{rT}$ and $\boldsymbol{\mu}_{rT}$ are the relative permittivity and permeability tensors at constant stress.

Because the in-plane dimensions of the antennas are much larger than their thickness, the displacement field and modal shape are nearly uniform in the azimuthal plane (i.e., we can assume that a pure thickness-extensional mode is excited [25]). We therefore retain only variations along the out-of-plane direction (z) and neglect in-plane derivatives [30]. This enables accurate extraction of all relevant quantities used to compute G_{ME} from a 2D cross-sectional FEM model. To do so, we simulate an arbitrarily wide cross-section with lateral continuity (periodic) boundary conditions, then post-process the strain-induced magnetization and fields from the resulting 2D solution. The simulation geometry and mesh are illustrated in Figure 4. A structured mesh of uniformly spaced rectangular elements is used, whose density was validated through a convergence study.

To quantify the gain reliably, it is necessary to accurately model the losses in the system, which originate from three main sources: (1) mechanical dissipation, quantified by the mechanical quality factor Q_m, (2) dielectric losses in the piezoelectric layer, determined by its loss tangent ($\tan\delta$), and (3) ohmic losses due to the finite conductivity of the electrodes. These loss contributions are lumped into the resistances R_m, R_0, and R_s of the MBVD equivalent circuit of the BAW resonator [22], and can be estimated by fitting the experimentally measured reflection coefficient of the devices, as shown in Figure 2a. The MBVD parameters from the fitting are reported in Table 1.

In the FEM model, mechanical and dielectric dissipation are accounted for by adding an imaginary term to the elasticity and permittivity matrices:

$$\begin{aligned} \mathbf{c}_E &\rightarrow (1 + j\,/Q_m)\,\mathbf{c}_E, \\ \boldsymbol{\epsilon}_{rT} &\rightarrow (1 - j\,\tan\delta)\,\boldsymbol{\epsilon}_{rT}. \end{aligned} \tag{4}$$

The effect of the series resistance R_s on the overall gain is instead incorporated in post-processing:

$$\begin{aligned} G_{\text{ME}} &= G_{\text{ME}}(R_s = 0) \cdot G_p \\ &= G_{\text{ME}}(R_s = 0) \cdot \frac{\text{Re}(Z_{\text{in}})}{R_s + \text{Re}(Z_{\text{in}})}, \end{aligned} \tag{5}$$

Table 1. Extracted MBVD Coefficients

Parameter	Unit	FeGaB	FeCoSiB
k_t^2	-	10%	10.7%
Q_m	-	100	100
$tan\delta$	-	0.02	0.025
R_m	Ω	0.727	0.546
R_s	Ω	16.6	13.7
L_m	nH	4.48	2.877
L_s	nH	0.138	0.15
C_m	pF	0.891	1.006
C_0	pF	11	11.6
R_0	Ω	0.115	0.125

where $G_{\text{ME}}(R_s = 0)$ and Z_{in} are the gain and the input impedance of the antenna extracted from the FEM simulation excluding R_s; G_p corresponds to the power gain of a two port network with only the resistance R_s connecting the two ports [31], capturing the reduction in the power delivered to the antenna caused by ohmic dissipations in R_s. In all simulations, the systems are excited by a $50\,\Omega$ source that provides a fixed incident power P_{inc}, part of which is absorbed, while the remaining part is reflected back to the source. This results in two distinct definitions of antenna gain, intrinsic and realized [32]. The intrinsic gain does not take the reflected power into account (or, in other terms, neglects impedance matching), and is given by the ratio of the radiated power to the absorbed power, times the directivity:

$$G_{\text{int}} = D \cdot \frac{P_{\text{rad}}}{P_{\text{abs}}} \tag{6}$$

The realized gain instead considers the ratio between the radiated and incident power, thus including the return loss:

$$G_{\text{realized}} = D \cdot \frac{P_{\text{rad}}}{P_{\text{inc}}} = G_{\text{int}} \cdot \left(1 - |S_{11}|^2\right). \tag{7}$$

In the next three sections, we start by considering the intrinsic gain for each radiation source first, then we will discuss impedance matching and realized gain.

All material parameters used in our simulations are listed in Table 2. We point out that the Young's moduli of FeGaB and FeCoSiB are fitted to match the measured resonance frequencies and electromechanical coupling values of the fabricated devices. This is necessary because the MS layer is in a remanent magnetization state during operation, which alters its elastic stiffness compared to the demagnetized state through the ΔE effect [19,33,34]. Since the magnitude of this shift depends on the specific magnetic state of the film and is not determined a priori, fitting the Young's moduli to the measured response provides a more accurate representation of the actual device behavior.

Method 1: magnetic-dipole (Larmor) formulation

In the first approach to extract G_{ME}, the MS layer is modeled as an electrically small magnetic dipole whose moment is obtained directly from the magnetization distribution computed by FEM. Specifically, for $\mathbf{m}(t) = \text{Re}\{\mathbf{m}_0 e^{j\omega t}\}$, the dipole moment is:

$$\mathbf{m}_0 = k_{eff} \int_{V_{\text{MS}}} \mathbf{M}(x, y, z)\, dV = k_{eff} \int_{V_{\text{MS}}} (\mathbf{B}/\mu_0 - \mathbf{H})\, dV, \tag{8}$$

where V_{MS} is the volume of the MS layer, and $k_{eff} = 0.9$ is a coefficient given by the ratio of the thickness of the magnetic material to the thickness of the non-magnetic one in the laminated MS stack, (see section III.A detailing the fabrication process). Since the enforced lateral strain uniformity makes the strain-driven AC magnetization uniform across the in-plane directions, the volume integral in Equation (8) can be rewritten as

$$\mathbf{m}_0 = \hat{\mathbf{x}} k_{eff} A_{\text{FBAR}} \int_{T_1} M(z)\, dz, \tag{9}$$

Table 2. Material Parameters Used in our FEM Simulations

Symbol	Quantity	Value
	Pt	
ρ	mass density	21 450 kg/m^3
E	Young's modulus	168 GPa
ν	Poisson's ratio	0.38
	AlScN[25,35]	
ρ	mass density	3 512 kg/m^3
c_{11}, c_{12}, c_{13} c_{33}, c_{44}, c_{66}	stiffness constants	332.6, 146.3, 134.3 GPa 241.1, 108.1, 92.65 GPa
e_{33}, e_{31}, e_{15}	piezoelectric constants	2.24, −0.72, −0.32 C/m^2
ε_r	relative permittivity	14.1
$\tan\delta$	loss tangent	0.025
Q_m	mechanical quality factor	100
	FeGaB[19][34]	
ρ	mass density	7 860 kg/m^3
E	Young's modulus	160 GPa
ν	Poisson's ratio	0.27
d_{33}	piezomagnetic constant	12 ppm/Oe
	FeCoSiB[19][34]	
ρ	mass density	7 250 kg/m^3
E	Young's modulus	150 GPa
ν	Poisson's ratio	0.30
d_{33}	piezomagnetic constant	5 ppm/Oe

where A_{ME} and T_1 are the in-plane area and thickness of the MS layer, respectively. Invoking the small dipole approximation, the time-averaged radiated power due to magnetoelastic coupling can therefore be expressed through Larmor's formula [36]:

$$P_{\mathrm{rad}}^{\mathrm{ME}} = 2\frac{\mu_0\omega^4|\mathbf{m}_0|^2}{12\pi c^3}. \tag{10}$$

The factor of 2 in Equation (10) accounts for the presence of the bottom Pt electrode, which acts as a ground plane. Since the induced magnetic dipole moment in the MS layer is in the plane of the film, by image theory this is equivalent to having a mirror image of the magnetization beneath the ground plane of equal magnitude, phase, and direction [32]. As the operating wavelength is much larger than the distance from the ground plane, the radiated fields generated by the dipole and its mirror image interfere constructively, doubling the radiated power and confining radiation to the half-space above the ground plane.

From the calculated $P_{\mathrm{rad}}^{\mathrm{ME}}$, the *intrinsic* gain is extracted as:

$$G_{\mathrm{ME}} = D \cdot \eta_{\mathrm{ME}} \cdot G_p = 3 \cdot \frac{P_{\mathrm{rad}}^{\mathrm{ME}}}{P_{\mathrm{abs}}} \cdot \frac{\mathrm{Re}(Z_{\mathrm{in}})}{R_s + \mathrm{Re}(Z_{\mathrm{in}})}, \tag{11}$$

where D is the directivity, η_{ME} is the radiation efficiency, and P_{abs} is the power absorbed at the device terminals (excluding R_s). Since radiation is confined to the upper half-space, the directivity is twice that of an electrically small dipole in free space, i.e. $D = 3$ [32].

The resulting G_{ME} vs. frequency curves are shown for both magnetostrictive materials in Figure 5. Although the intrinsic gain does not take impedance matching into account, for both antennas the gain peaks at the respective anti-resonance frequency. This is due to the fact that G_p, which accounts for the ohmic dissipation in the overall gain, is the highest at f_p, where the impedance of the resonators is the largest (thus, where ohmic dissipations in R_s are the lowest). We note that the FeCoSiB-based device operates at a higher frequency compared to the FeGaB-based one (3.08 GHz vs. 2.62 GHz) and has a slightly higher k_t^2 (10.7% vs. 10%). This is due to the FeCoSiB film having a lower mass density compared to FeGaB.

Method 2: equivalence-principle formulation

The gain G_{ME} can also be evaluated using an equivalence-principle formulation. When the distance of the MS layer from the ground plane is much smaller than the wavelength, the antenna can be modeled by an equivalent magnetic surface current [37]:

$$\mathbf{M}_{\mathrm{surf}} = -2\,\hat{\mathbf{n}} \times \mathbf{E}, \tag{12}$$

where $\hat{\mathbf{n}}$ is the outward unit normal and $\mathbf{E}$ is obtained from the FEM solution. The factor of 2 accounts for the image contribution. Assuming a circular radiating aperture of radius $a = D_1/2$ (see Figure 1a) with uniform excitation over the disk, the far-field can be evaluated analytically using a Green function formalism in a spherical coordinate system [32][38]:

$$\begin{aligned} E_\theta(r,\theta,\phi) &= \frac{jka^2\,e^{-jkr}}{r}\ \sin\phi\ F(\theta), \\ E_\phi(r,\theta,\phi) &= \frac{jka^2\,e^{-jkr}}{r}\ \cos\theta\cos\phi\ F(\theta), \\ F(\theta) &= E_{\mathrm{t}}\,\frac{2J_1(ka\sin\theta)}{ka\sin\theta}, \end{aligned} \tag{13}$$

where $k = \omega/c$ is the free-space wavenumber, and $J_1(\cdot)$ is the Bessel function of the first kind of order one. The quantity E_{t} denotes the magnitude of the tangential electric-field component on the top surface of the MS layer.

The time-averaged Poynting vector is then:

$$\langle \mathbf{S} \rangle = \frac{(ka^2 E_{\mathrm{t}})^2}{2\eta_0 r^2}\left(\sin^2\phi + \cos^2\theta\cos^2\phi\right)\left[\frac{J_1(ka\sin\theta)}{ka\sin\theta}\right]^2 \hat{\mathbf{r}}, \tag{14}$$

and the radiated power is obtained by numerically integrating over the upper half-space:

$$P_{\mathrm{rad}}^{\mathrm{ME}} = \int_0^{2\pi}\int_0^{\pi/2} \langle \mathbf{S} \rangle \cdot \hat{\mathbf{r}}\ r^2 \sin\theta\, d\theta\, d\phi. \tag{15}$$

While in the previous section we assumed the maximum directivity to be $D = 3$, here Eq. 15 allows the directivity to be calculated through its definition:

$$D(\theta,\phi) = \frac{4\pi r^2 \langle \mathbf{S} \rangle}{P_{\mathrm{rad}}^{\mathrm{ME}}}. \tag{16}$$

Its maximum value is $D(\theta = \pi/2, \phi = 0) = 3$, consistent with the small dipole approximation made in the previous section. From Equation (11), we can once again compute G_{ME}, whose frequency trend is also reported in Figure 5. This trend agrees with the one obtained using Method 1, confirming the equivalence of the two methods.

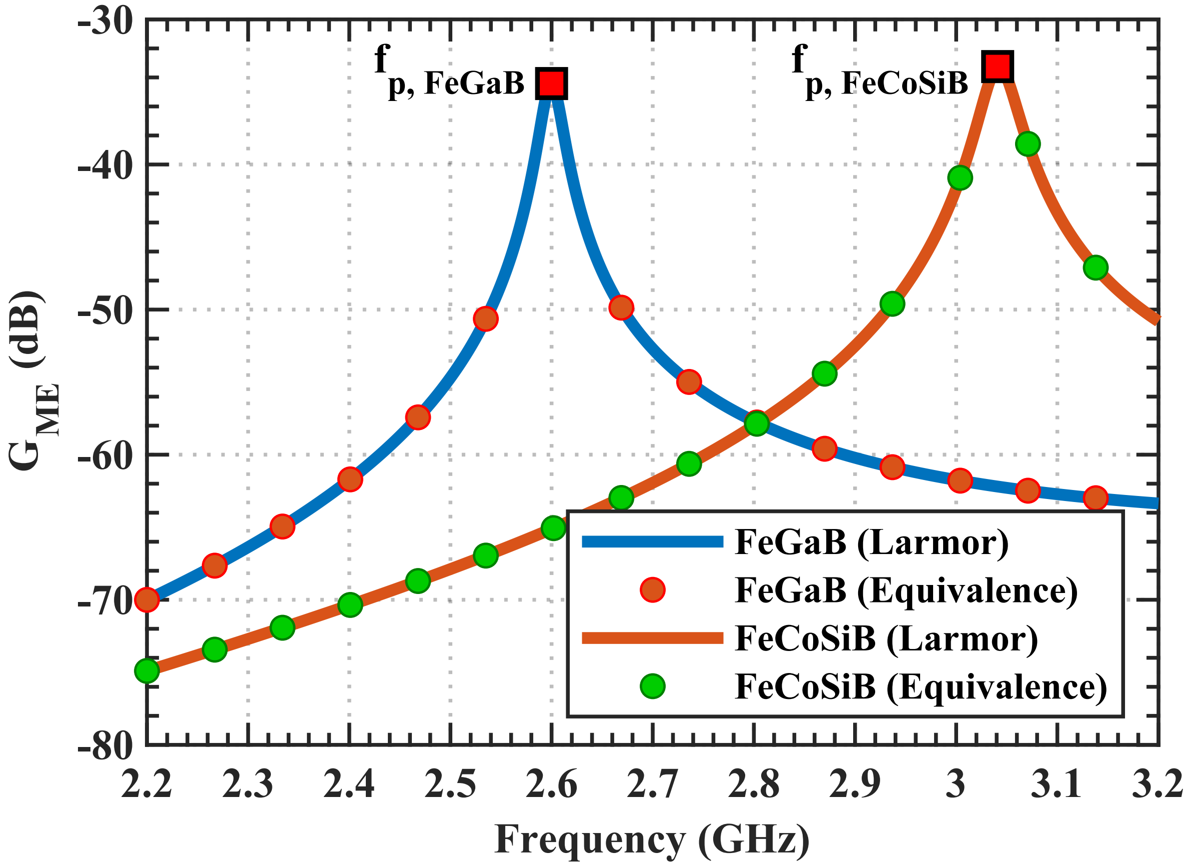

Figure 5. G_{ME} versus frequency, computed using the Larmor (dipole-moment) method and the equivalence-principle method for the FeGaB-based and FeCoSiB-based BAW ME antennas. We note the equivalence of the two methods used to model G_{ME}, which identify a maximum G_{ME} of -34 dB and -33 dB for FeGaB and FeCoSiB, respectively.

2.2. Radiation from Equivalent Magnetic Currents

A BAW resonator, even when not loaded with a magnetic material, effectively behaves as a small electric dipole, and thus radiates electromagnetic waves. The total electric dipole moment is given by two distinct contributions: one from the charges on the top and bottom electrodes, the other from the strain-driven electric polarization $\mathbf{P} = \mathbf{d}^T\mathbf{E}$ within the piezoelectric material. Both contributions can be taken into account by treating the resonator as an electrically small microstrip antenna over a piezoelectric substrate and employing the surface equivalence principle [39]. To do so, we consider an imaginary cylindrical surface S that encloses the piezoelectric layer; the equivalent magnetic current density is given by $\mathbf{J}_m = \mathbf{E} \times \hat{\mathbf{n}}$, where $\hat{\mathbf{n}}$ is the outward surface normal to S. Since $\mathbf{E}$ is normal to the electrodes, which we approximate as perfect electric conductors, $\mathbf{J}_m$ is non-zero only on the lateral edges of S. Neglecting the fringing fields, the total magnetic current becomes:

$$\begin{aligned} \mathbf{I}_m &= \int_0^{T_2} \mathbf{J}_m \, dz = \int_0^{T_2} \mathbf{E} \times \hat{\mathbf{n}} \, dz \\ &= (\hat{\mathbf{z}} \times \hat{\mathbf{n}}) \int_0^{T_2} E_z \, dz = -V(\hat{\mathbf{z}} \times \hat{\mathbf{n}}), \end{aligned} \tag{17}$$

where T_2 is the thickness of the piezoelectric layer, and V is the voltage across the device, which can be extracted from the same multiphysics FEM model detailed in the previous section. The corresponding dipole moment is

$$\mathbf{p_0} = A_{FBAR} I_m \hat{\mathbf{z}}, \tag{18}$$

and its radiated power can be found through Larmor's formula for an electrically small magnetic current loop parallel to a ground plane [36]:

$$P^{m}_{\rm rad} = 2\frac{\epsilon_0 \omega^4 |\mathbf{p_0}|^2}{12\pi c^3}. \tag{19}$$

The directivity can be assumed to be twice that of a point dipole in free space, $D = 3$; thus, the corresponding intrinsic gain component G_m is given by

$$G_m = D \cdot \eta_m \cdot G_p = 3 \cdot \frac{P^{m}_{rad}}{P_{abs}} \cdot \frac{\mathrm{Re}(Z_{\rm in})}{R_s + \mathrm{Re}(Z_{\rm in})}, \tag{20}$$

whose behavior versus frequency is shown in Figure 6 for both antennas.

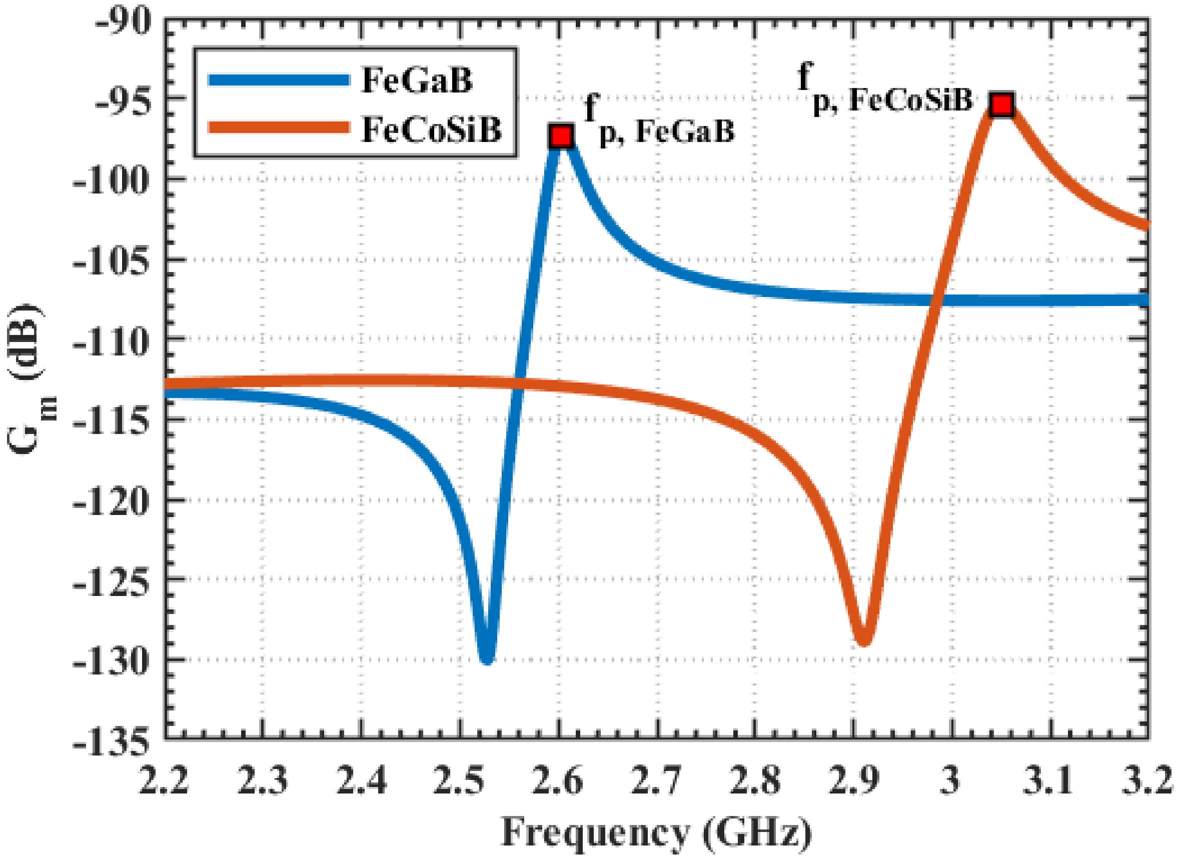

Figure 6. G_m versus frequency for the FeGaB-based and FeCoSiB-based BAW ME antennas. A maximum G_c of -98 dB and -95 dB is extracted for FeGaB and FeCoSiB, respectively, which is several orders of magnitude lower than $G_{\rm ME}$.

This gain contribution shows a dip at the resonance frequency, where the admittance of the resonator is highest, and hence the induced voltage is lower, and a peak at the anti-resonance frequency, where the reverse holds. It is also worth mentioning that the gain profile does not depend on the magnetic properties of the specific MS layer, as $\mathbf{p}_0$ depends only on the device area and on the input voltage, which, for a given input power, is determined by the admittance of the resonator. Thus, the difference between G_m for FeGaB-based and FeCoSiB-based antennas is due only to their different MBVD parameters. In particular, where the $|S_{11}|$ is minimum, both devices act approximately as $50\,\Omega$ loads, and the difference in G_m is given by the ratio of their respective anti-resonance frequencies: $3.08^4/2.62^4 \approx 3\,\mathrm{dB}$.

Importantly, we notice that G_m sits below -90 dB over the entire frequency range, approximately 60 dB lower than the magnetoelastic gain, proving that this source is not the main gain contribution for BAW ME antennas.

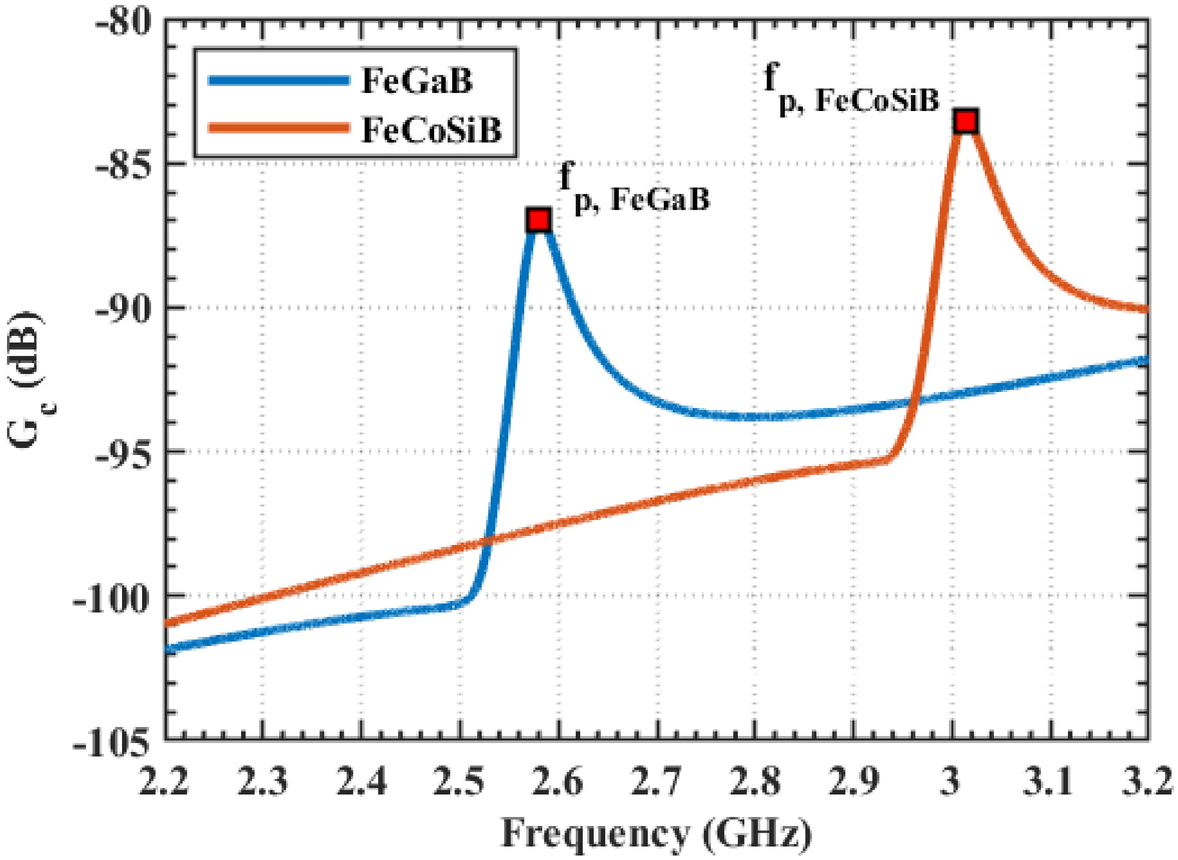

Figure 7. G_c versus frequency for the FeGaB-based and FeCoSiB-based BAW ME antennas. A maximum G_c of -87 dB and -83 dB is extracted for FeGaB and FeCoSiB, respectively, which is several orders of magnitude lower than G_{ME}.

2.3. Radiation from Electrical Currents in the Probing Pads

A portion of the radiated power can arise from the electric current flowing through the probing pads, as in a conventional EM antenna. This current can be split in three components: a current i_1 flowing in the signal pad and through the via that connects it to the bottom Pt electrode, and two identical return currents $i_2 = i_3 = i_1/2$ flowing on the left and right side of the ground pad, shown graphically in Figure 3.

Due to the symmetric structure of the pads and of the excitation, the net dipole moment of the current distribution is zero. Therefore, we anticipate both the radiated power associated with these currents, P^c_{rad}, and the corresponding gain contribution, G_c, to be modest since only the higher-order multipole terms, which radiate more weakly, survive. However, evaluating G_c is necessary to quantitatively compare this radiation mechanism with other ones present in BAW ME antennas. To this end, we use a full-wave electromagnetic solver to simulate the radiation from the current distribution on the probing pads, considering the same geometry shown in Figure 1a. Since conventional electromagnetic simulations do not take into account the acoustic behavior of the FBAR, we replace the latter with an equivalent lumped impedance element between the signal and ground pads, whose element values are the same as those of the MBVD circuit model (see Table 1). This ensures that the current density on the pads matches the real scenario, and also ensures that mechanical, dielectric, and ohmic losses are included all at once when the gain is computed.

The simulated intrinsic gain G_c trend versus frequency is shown in Figure 7. For both antennas, G_c peaks at the respective anti-resonance frequency. Similarly to G_m, the gain component G_c is independent of the magnetic properties of the MS layer, as they do not affect the current distribution on the pads. The difference in G_c for the FeGaB and FeCoSiB-based antennas is thus only due to their different admittance profiles. While there is no analytic formula for P^c_{rad}, it is reasonable to assume that it monotonically increases with frequency, as is the case for P^{ME}_{rad} and P^m_{rad}, which would account for the higher (by $\sim 3\,$dB) peak value of G_c of FeCoSiB compared to FeGaB.

As anticipated, G_c remains lower than -80 dB across the entire frequency span, leading to the conclusion that G_c is also not the main source of gain for BAW ME antennas.

2.4. Total Realized Gain

In the preceding three sections, the radiated power and the corresponding gain have been calculated assuming each source to be acting in isolation. In general, when two sources in free space produce electric fields $\mathbf{E_1}$ and $\mathbf{E_2}$, the total field is $\mathbf{E}_{\text{tot}} = \mathbf{E_1} + \mathbf{E_2}$ by the superposition principle, and the Ponyting vector in the far-field is:

$$\langle \mathbf{S} \rangle = \frac{|\mathbf{E}_{\text{tot}}|^2}{2\eta_0}\hat{\mathbf{r}} = \frac{|\mathbf{E}_1 + \mathbf{E}_2|^2}{2\eta_0}\hat{\mathbf{r}} = \frac{1}{2\eta_0}(\mathbf{E}_1 + \mathbf{E}_2 + 2\mathbf{E}_1 \cdot \mathbf{E}_2)\hat{\mathbf{r}}. \tag{21}$$

The total radiated power, obtained by integrating the Poynting vector over a closed spherical surface, is:

$$\begin{aligned} P^{\text{tot}}_{\text{rad}} &= \oint \frac{|\mathbf{E}_1|^2}{2\eta_0}\hat{\mathbf{r}} \cdot d\mathbf{S} + \oint \frac{|\mathbf{E}_2|^2}{2\eta_0}\hat{\mathbf{r}} \cdot d\mathbf{S} + \oint \frac{2\mathbf{E}_1 \cdot \mathbf{E}_2}{2\eta_0}\hat{\mathbf{r}} \cdot d\mathbf{S} \\ &= P_1 + P_2 + P_{\text{int}}, \end{aligned} \tag{22}$$

where P_1 and P_2 are the powers radiated by the two sources isolated, and P_{int} is a term that quantifies the interference between them. When the surface integral of $\mathbf{E}_1 \cdot \mathbf{E}_2$ is zero, $P_{int} = 0$ and the total radiated power reduces to the sum of the individual contributions.

In our case, since $P^{\text{ME}}_{\text{rad}} \gg P^m_{\text{rad}}, P^c_{\text{rad}}$, the fields associated with the equivalent magnetic currents and with the pad currents can be assumed to be negligible compared to those arising from magnetoelastic coupling. Therefore, both their individual radiated powers and the relative interference terms can thus be assumed to be correspondingly small. Actually, since the magnetic dipole moment $\mathbf{m_0}$ and the electric dipole moment $\mathbf{p_0}$ are orthogonal, for them $P_{int} = 0$ exactly. The interference from the currents on the probing pads is more difficult to evaluate, since there is no closed-form expression for the electric field they generate, but can still be neglected due to what has been said above. In conclusion, the total radiated power and intrinsic gain can be reliably approximated by just the magnetoelastic component:

$$P^{tot}_{rad} \approx P^{\text{ME}}_{\text{rad}} \implies G_{tot} \approx G_{ME}. \tag{23}$$

So far, only the intrinsic gain has been considered. To take into account the losses from impedance mismatch, discussed in the next section and as done in our measurements, we compute and plot the *realized* gain as well:

$$G^{realized}_{tot} = G_{tot} \cdot \left(1 - |S_{11}|^2\right) \tag{24}$$

The simulated trend of $G^{realized}_{tot}$ versus frequency is shown in Figure 8 for both the FeGaB-based and the FeCoSiB-based antennas. As expected, the curves of the total realized gain and the intrinsic magnetoelastic gain in Figure 5 are nearly equal, due to the magnetoelastic component being dominant and to the high return loss of the devices across the whole frequency range. Moreover, the peak gain reaches a value of approximately -35 dB when using FeGaB as the MS and -34 dB when using FeCoSiB, comparable to the experimentally measured values (see section III.B).

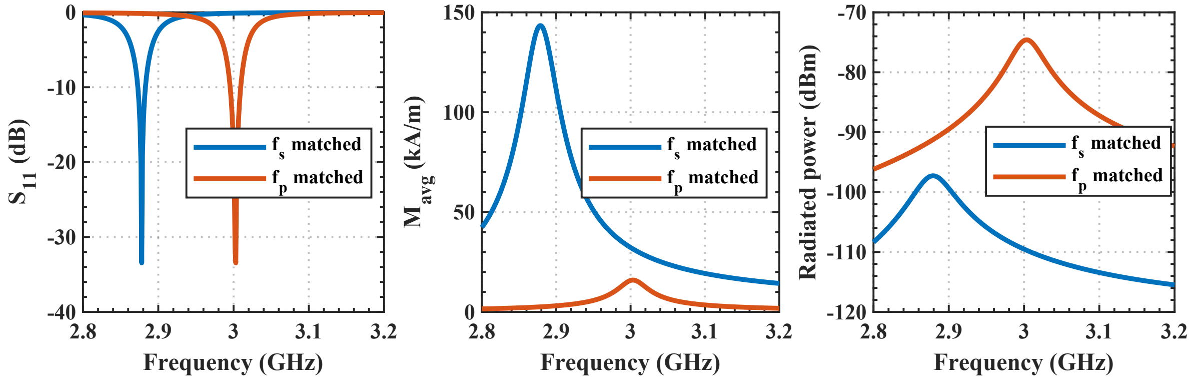

Figure 9. Comparison of the antenna performance for resonance-matching and anti-resonance-matching conditions: (a) return loss; (b) average magnetization magnitude; (c) radiated power versus frequency. Simulation were performed for the FeCoSiB design when using an input power of 1 μW.

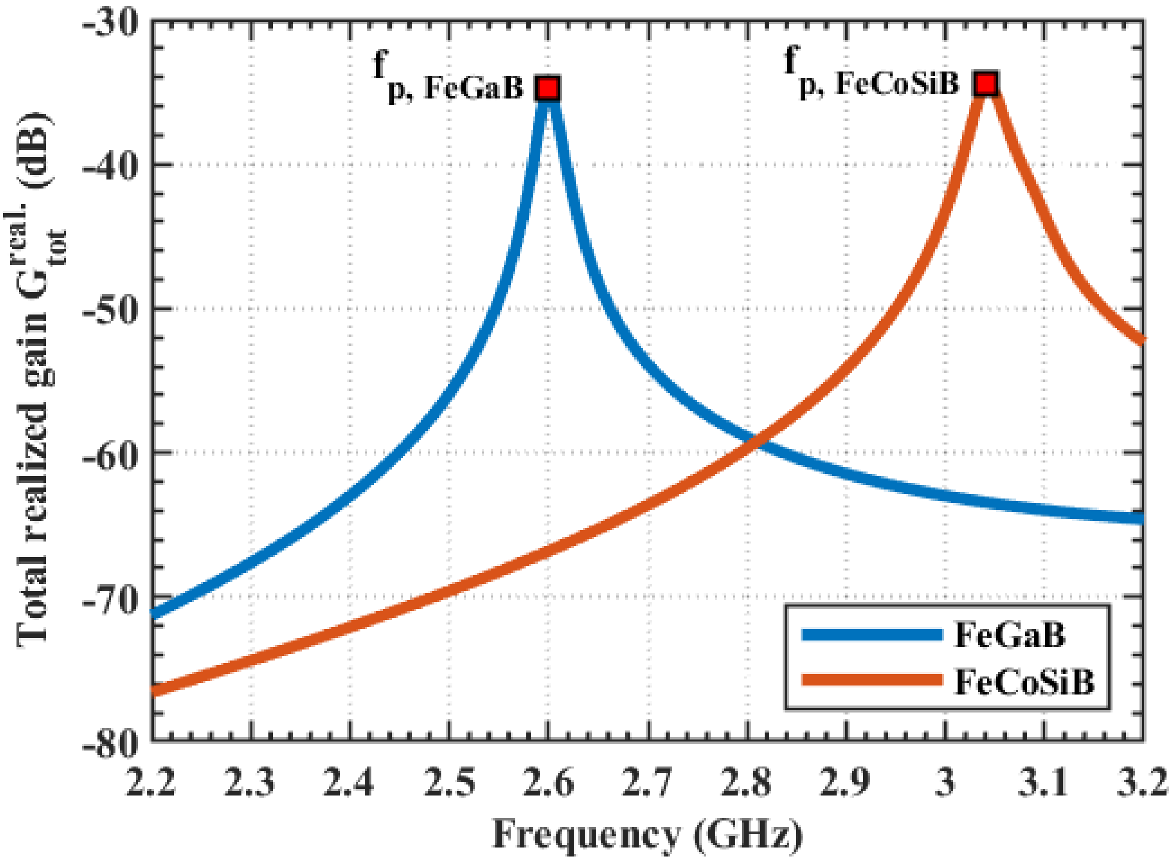

Figure 8. Total realized gain versus frequency for the FeGaB-based and FeCoSiB-based BAW ME antennas, obtained by summing the contributions from all three sources described in Sections A to C.

2.5. Impedance Matching

Impedance matching is one of the key issues with conventional electrically-small antennas. When the linear size of an antenna is much smaller than the operating wavelength, the reactive part of the impedance dominates over the radiation resistance, rendering a matching network necessary to obtain maximum power transfer. However, designing one presents several challenges. First, matching an impedance with a large reactance and low resistance to a reference impedance (most often $Z_{\text{ref}} = 50\,\Omega$) requires a network with a high quality factor, which is difficult to obtain with lumped elements. Secondly, real matching networks can have parasitic resistances comparable or greater than the radiation resistance of electrically small antennas, further lowering their efficiency.

Acoustically-actuated antennas overcome these issues by operating at the acoustic resonance, which, due to the speed of sound being much lower than that of electromagnetic waves, occurs at much larger frequencies. The motional branch of the resonator can thus effectively work as a matching network for the antenna. Specifically, impedance matching can be obtained in two ways. The first is by matching the resonator to $Z_{\text{ref}} = 50\,\Omega$ at the mechanical series resonance frequency, given by $\omega_s = 1/\sqrt{L_m C_m}$. At this frequency, the reactances of the motional inductance L_m and capacitance C_m cancel out, and the mechanical response of the system reaches its maximum amplitude. When $1/\omega_s C_0 \ll R_m$, the total impedance of the resonator is approximately equal to R_m, which is given by [40]:

$$R_m = \frac{\pi^2}{8}\frac{1}{\omega_s C_0 k_t^2 Q_m}, \tag{25}$$

Since the static capacitance is proportional to the area of the device A_{FBAR}, the latter can be sized to give $R_m = 50\,\Omega$, corresponding to

$$C_0 = \frac{\pi^2}{8}\frac{1}{\omega_s k_t^2 Q_m \cdot 50\,\Omega}. \tag{26}$$

An alternative strategy, which has been exploited in this work, is to match the device at its parallel resonance frequency, or anti-resonance, which is found at $\omega_p \approx \omega_s\sqrt{1 + C_m/C_0}$. In this case, the reactance of the static branch cancels the reactance of the motional branch, yielding a purely real impedance. For low loss substrates[41], this is approximately:

$$R_p \approx \frac{8}{\pi^2}\frac{Q_m k_t^2}{\omega_s C_0}. \tag{27}$$

As in the previous case, the area of the device, and therefore C_0, can be determined to obtain $R_p = 50\,\Omega$:

$$C_0 \approx \frac{8}{\pi^2}\frac{Q_m k_t^2}{\omega_s \cdot 50\,\Omega}. \tag{28}$$

Equations (26, 28) neglect the ohmic and dielectric losses in the resonator, as well as the stray inductance of the contacting pads. While accurate design requires accounting for these non-idealities, the above expressions provide useful first-order estimates for device sizing.

To compare the two options, we first note that matching at series resonance maximizes the mechanical stress in the MS layer, resulting in a larger magnetization response. For a given absorbed power, the stress at ω_s is enhanced by approximately a factor of $Q_m k_t^2$ compared to operation at anti-resonance. However, as evident from (26) and (28), achieving matching at ω_s requires a value of C_0 that is smaller by a factor of $(\frac{8}{\pi^2} Q_m k_t^2)^2$ relative to that required for matching at ω_p. Since $C_0 \propto A_{\text{FBAR}}$, this implies that anti-resonance matching leads to devices that must be enlarged by the same factor. Because the total magnetic moment $\mathbf{m}$ scales linearly with both the device area and the stress in the MS layer, and the radiated power follows $P_{\text{rad}}^{\text{ME}} \propto |\mathbf{m}|^2$, the increased area compensates for the reduced stress. Overall, the radiated power scales proportionally to $\sim Q_m^2 k_t^4$ in favor of anti-resonance matching.

To validate this analysis, we simulate two devices that differ only in area, chosen to achieve identical return loss: one matched at resonance and the other at anti-resonance (Figure 9a). We show results for FeCoSiB only for clarity, as the conclusions are valid independently of the material. Assuming the same electromechanical parameters obtained from our fitting, $Q_m = 100$ and $k_t^2 = 10.7\%$ (see Table 1), and applying an input power $P_{\text{in}} = 1\,\mu\text{W}$, the resonance-matched device reaches an average magnetization of $M_{\text{avg}} \approx 140\,\text{kA/m}$, whereas the anti-resonance-matched device achieves $M_{\text{avg}} \approx 16\,\text{kA/m}$, as seen in Figure 9b. Despite this reduced magnetization, the larger device area results in a radiated power approximately 23 dB higher for the anti-resonance case (Figure 9c). Therefore, although anti-resonance matching reduces the mechanical and magnetic response, we found that this reduction is largely offset by the increased device size, ultimately leading to improved radiation performance. To the best of our knowledge, this trade-off has not been previously recognized in the literature, and represents a novel design insight for ME antennas. Guided by this finding, we adopted anti-resonance matching for the AlScN-based BAW ME antennas developed in this work.

2.6. Impact of the Scandium Doping Concentration

The use of heavily Sc-doped AlScN is motivated by its enhanced piezoelectric coefficients, which yield a higher k_t^2 [42]. Figure 10 shows the simulated variation of k_t^2 with increasing Sc-doping concentration. When there is no doping, i.e. the material is pure AlN, $k_t^2 \approx 5\%$; for 30% doping concentration, $k_t^2 \approx 11\%$, consistent with our measured response. Increasing the concentration to 40% could potentially boost the k_t^2 to 17.5%. To understand the role this parameter plays in determining both the gain and the -10 dB fractional bandwidth of the antenna, we carry out simulations in two distinct scenarios, using the FeCoSiB antenna as a reference.

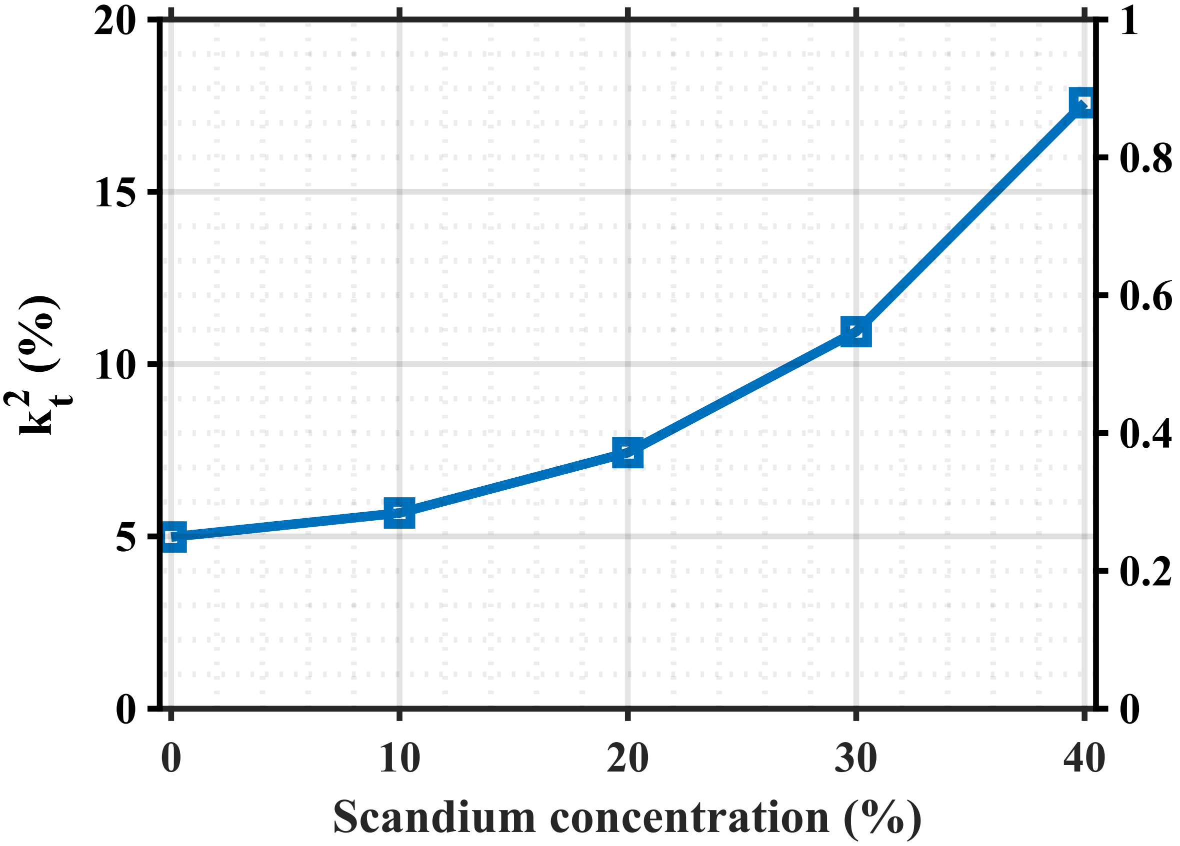

Figure 10. Electromechanical coupling versus Sc-doping concentration in the AlScN film. The study is performed assuming the variation in Sc-doping concentration for the FeCoSiB design.

In the first scenario, the Sc-doping concentration is varied while the return loss is held constant by simultaneously adjusting the device area. From Equation 28, $C_0 \propto k_t^2$, and since $C_0 \propto A_{\text{FBAR}}$, the device area scales linearly with k_t^2. Because the radiated power scales as A_{FBAR}^2, the gain increases as $\left(k_t^2\right)^2$. The -10 dB fractional bandwidth, however, is set by the FBAR's electromechanical response and remains largely unaffected by the area adjustment, as shown in Figure 11.

In the second scenario, the Sc-doping concentration is varied while the device area is fixed at its nominal value $A_{FBAR} = \pi D_1^2/4$, with $D_1 = 200\,\mu$m (see Figure 1. In this case, the impedance matching degrades as k_t^2 deviates from its nominal value, worsening the return loss. However, as long as an acceptable 50 Ω matching is still achieved, the -10 dB fractional bandwidth increases monotonically with k_t^2, as illustrated in Figure 12).

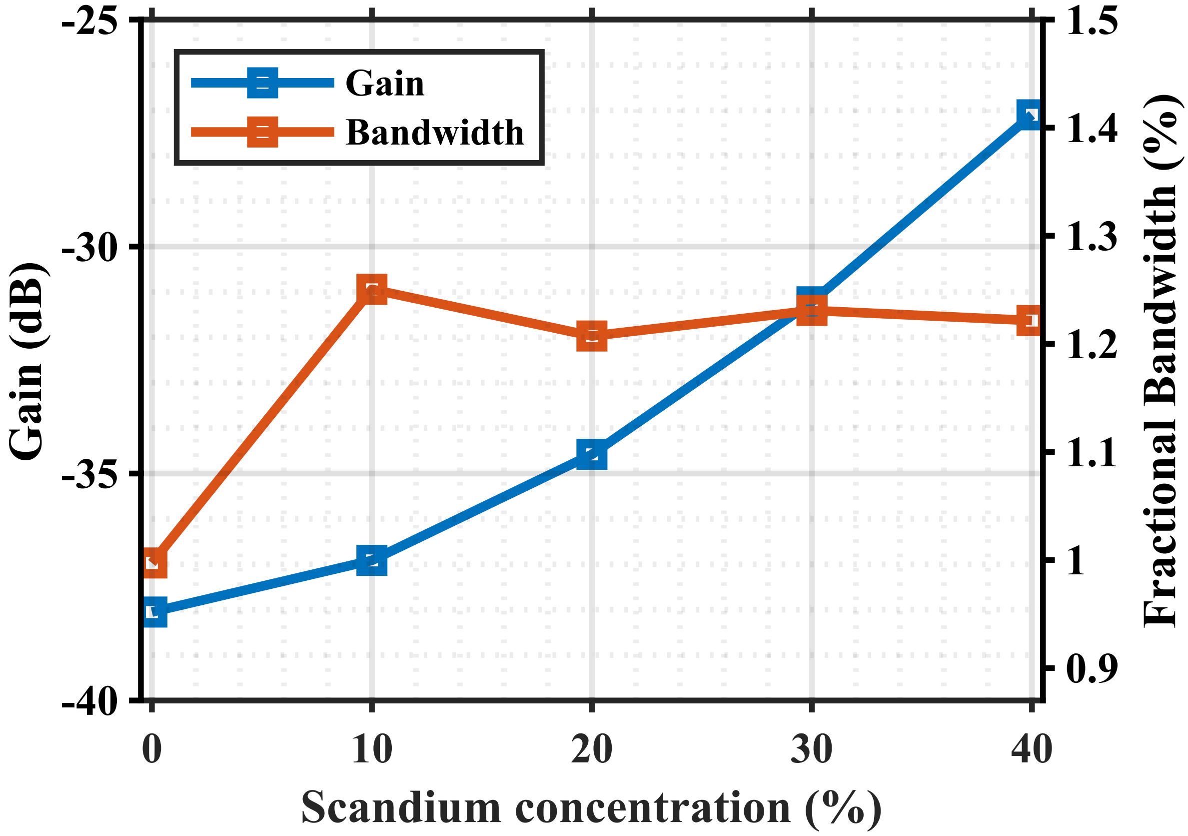

Figure 11. Simulated gain and -10 dB fractional bandwidth versus Sc-doping concentration, with device area adjusted to maintain constant return loss. The study is performed assuming the variation in Sc-doping concentration for the FeCoSiB design.

Together, these two scenarios show that the higher k_t^2 enabled by AlScN simultaneously improves the gain (when the device is properly sized) and widens the -10 dB fractional bandwidth, making it the key material advantage of this piezoelectric substrate.

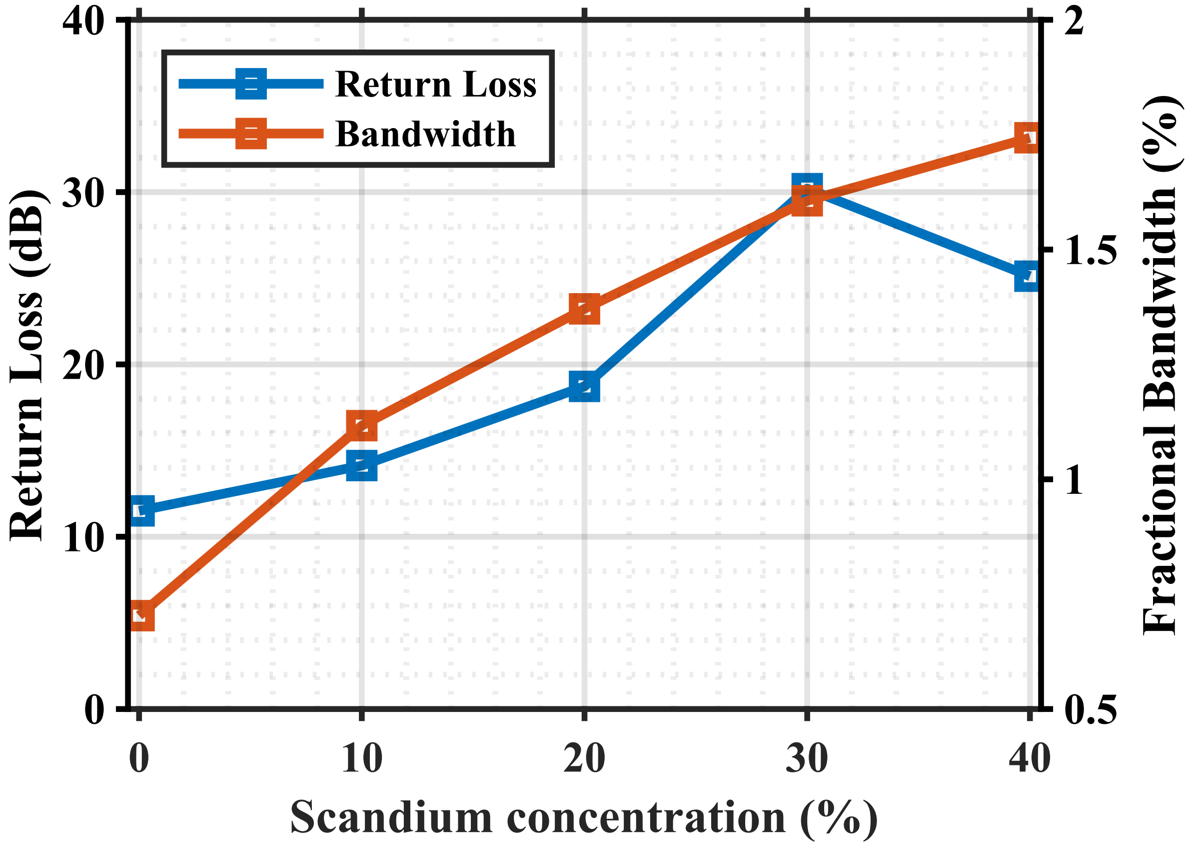

Figure 12. Simulated return loss and -10 dB fractional bandwidth versus Sc-doping concentration of the AlScN film, with device area held constant at its nominal value, $A_{FBAR} = \pi D_1^2/4$, with $D_1 = 200\,\mu$m (see Figure 1. The study is performed assuming the variation in Sc-doping concentration for the FeCoSiB design.

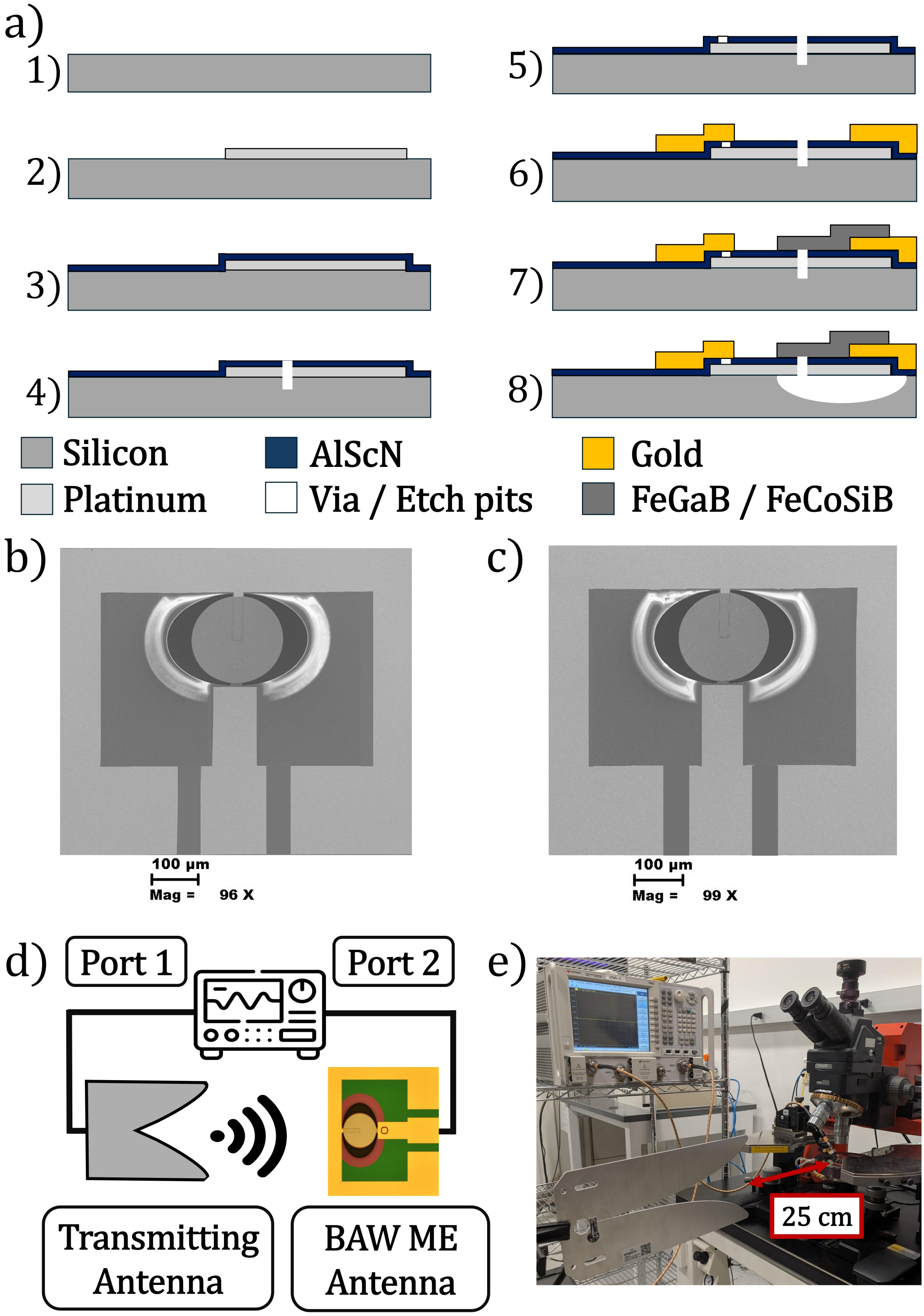

Figure 13. a) Fabrication process used for the BAW ME antennas built in this work. b, c) SEM pictures of the FeGaB-based (b) and FeCoSiB-based (c) fabricated AlScN-based BAW ME antennas. d) Illustration and e) picture of the experimental set-up used to characterize the gain of the BAW ME antennas. The device under test is connected to a VNA with a transmitting antenna with fully characterized gain, and the two antennas are positioned at a fixed distance of 25 cm.

doi:10.20944/preprints202605.0722.v1

3. Fabrication and Measured Results

3.1. Fabrication Process

The fabrication process of the antennas is outlined in Figure 13a. A 10 nm-thick titanium (Ti) adhesion layer is sputtered on a 500 μm-thick high resistivity (HR) silicon wafer. Then, a 80 nm-thick platinum (Pt) bottom electrode is deposited through RF sputtering, for which we developed a bi-layer lift-off process to minimize fencing effects along the edges of the bottom electrode [43,44]. The 500 nm-thick AlScN layer is subsequently deposited through magnetron sputtering. The AlScN deposition conditions have been optimized on an industrial-grade Evatec® Clusterline 200 in conjunction with a 12-inch alloy casted target. The etch pits and a via are then etched in the piezoelectric film through Ion Beam Etching (IBE) and wet etch, respectively. Subsequently, a 150 nm-thick Gold (Au) top electrode is deposited through e-beam evaporation, and the MS layer (a 500 nm-thick FeGaB or FeCoSiB layer) is then deposited via DC sputtering. To reduce eddy currents that would affect the gain of our antennas, the MS film is laminated with thin layers of insulating material [45]. In this regard, the MS layer consists of a stack of ten 45 nm thick FeGaB or FeCoSiB layers, each capped by a 5 nm thick Al_2O_3 film. In order to pre-orient the magnetic domains and induce a uniaxial in-plane anisotropy, we applied a 100 Oe in-situ magnetic field perpendicular to the direction of the anchors during the sputtering deposition [46]. Finally, a 10 nm thick Aluminum capping layer is deposited to protect the MS stack from XeF_2, which was used to release the FBAR structure [46]. To experimentally validate the role that the acoustic branch plays in the gain enhancement of ME antennas, we also fabricated and characterized devices identical to the two BAW antennas but left them unreleased. Figures 13b and c report Scanning Electron Microscope (SEM) picture of the FeGaB-based and FeCoSiB-based microfabricated released devices, respectively.

3.2. Antenna Measurements

The realized gain of the fabricated devices is characterized in an uncontrolled electromagnetic environment through direct wafer probing, using a GSG probe with a 150 μm pitch. The S-parameters are recorded with a Keysight N5221A Vector Network Analyzer (VNA).

The experimental setup for gain extraction is illustrated in Figure 13d,e. A transmitting Vivaldi antenna (RFSPACE UWB-3) is placed at a fixed distance of 25 cm from the device under test and connected to port 1 of the VNA, while port 2 is connected to the on-chip receiving antenna via GSG probes. The antenna's realized gain is extracted using the gain transfer method [10] [32], in which a reference antenna of known gain G_{REF} replaces the on-chip antenna:

$$G_{ME} = G_{REF} + 20\log_{10}(|S_{21,ME}|) - 20\log_{10}(|S_{21,REF}|), \tag{29}$$

where $S_{21,ME}$ and $S_{21,REF}$ are the transmission coefficients in linear scale measured with the BAW ME antenna and the reference antenna in place, respectively.

doi:10.20944/preprints202605.0722.v1

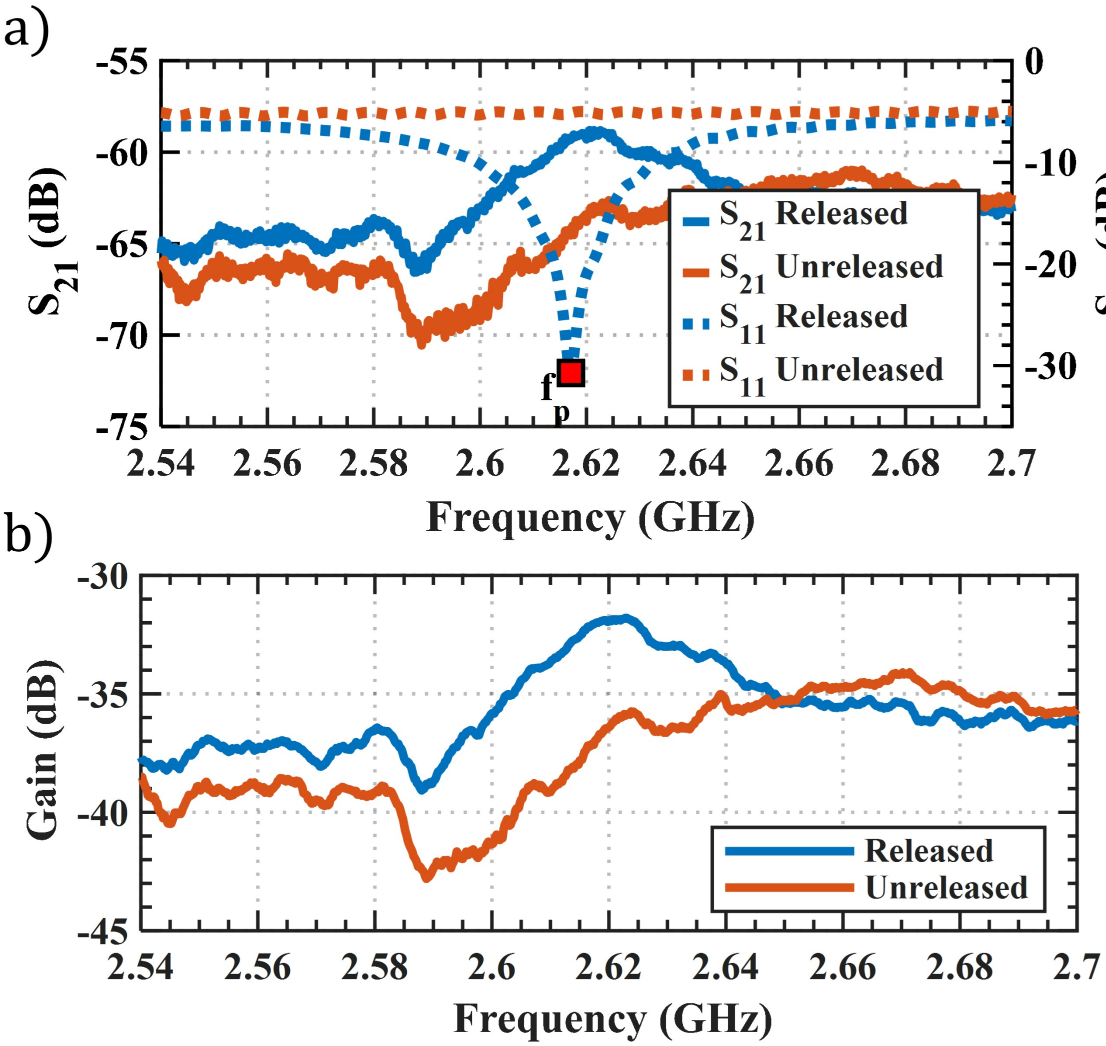

Figure 14. Experimentally extracted a) S_{21} versus frequency trend for the FeGaB-based released and unreleased BAW ME antennas. We also report the S_{11} of both released and unreleased devices, showing that the maximum value of the S_{21} is closely aligned to the f_p of the device. b) Realized gain of the FeGaB-based BAW ME antenna. A boost in radiation is visible at the f_p of the main mode of the device (2.62 GHz), corresponding to a maximum gain value of -31.8 dB.

doi:10.20944/preprints202605.0722.v1

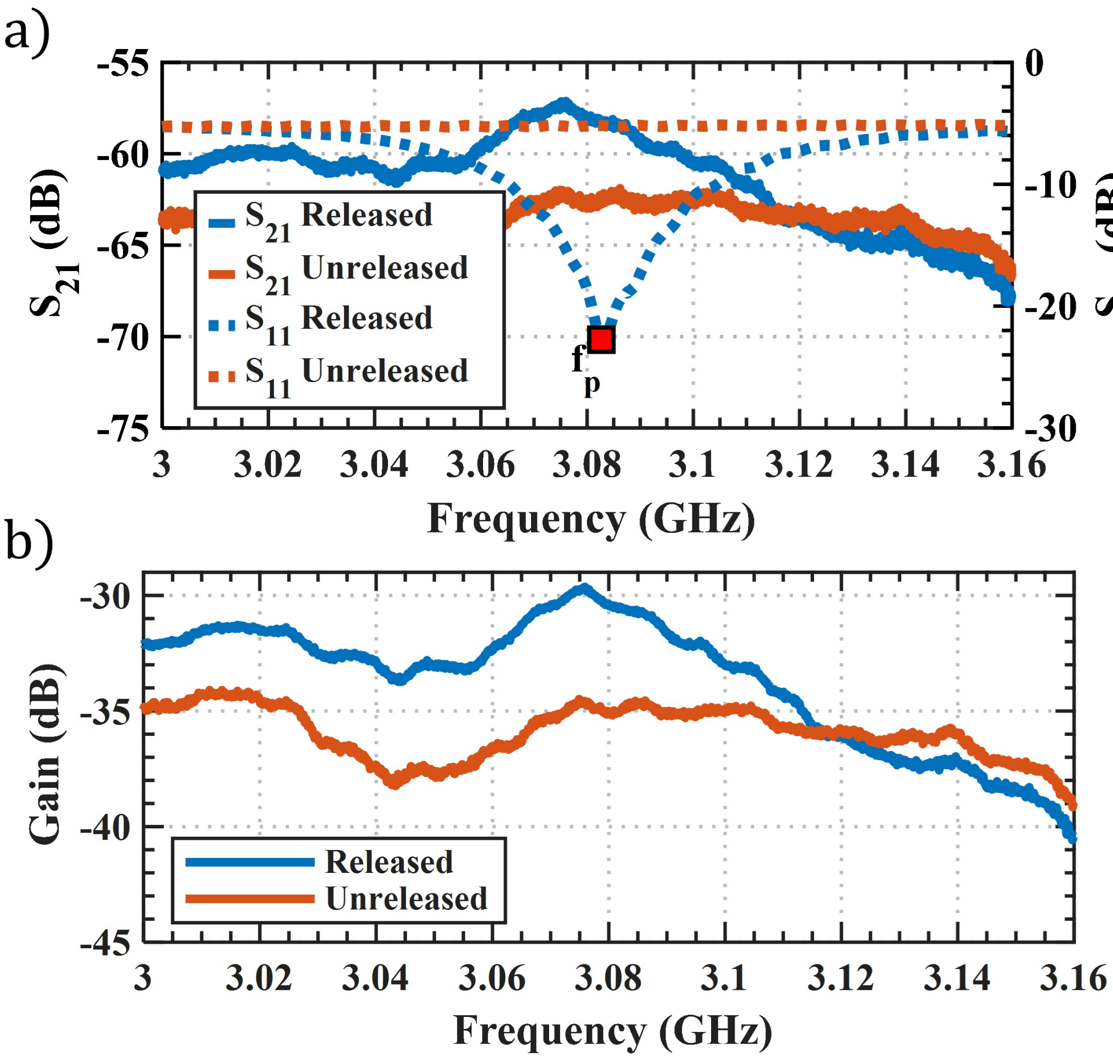

Figure 15. Experimentally extracted a) S_{21} versus frequency trend for the FeCoSiB-based released and unreleased BAW ME antennas. We also report the S_{11} of both released and unreleased devices, showing that the maximum value of the S_{21} is closely aligned to the f_p of the device. b) Realized gain of the FeCoSiB-based BAW ME antenna. A boost in radiation is also visible at the f_p of the device (3.08 GHz), corresponding to a maximum gain value of -29.7 dB.

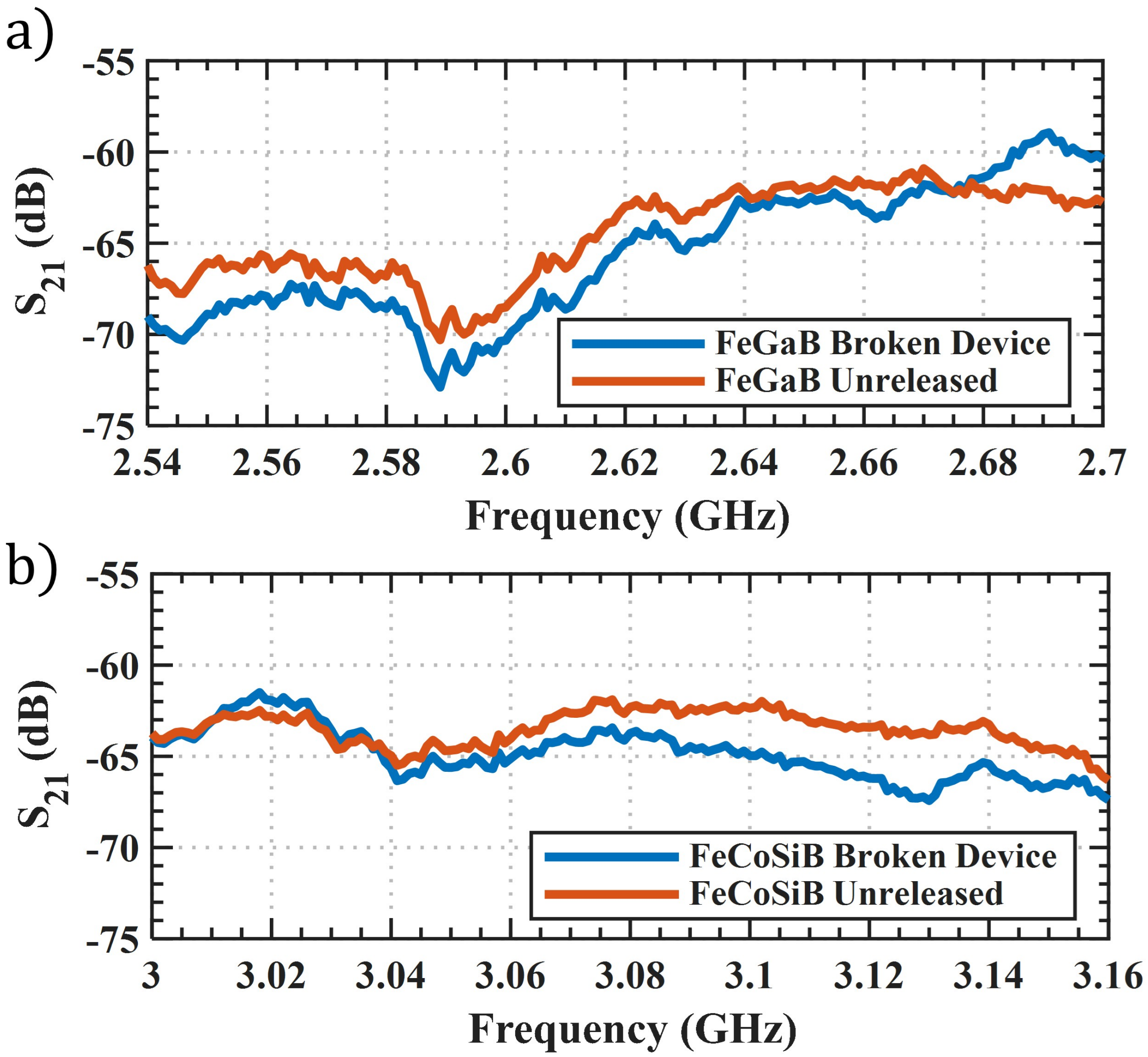

Figure 16. Experimental S_{21} parameters extracted for the unreleased and broken devices for both the FeGaB (top) and FeCoSiB (bottom) antennas.

Table 3. Comparison Between Different BAW ME Antennas.

Work	Material	Type	Technology	Frequency (GHz)	Gain (dB)	k_t^2	Fractional Bandwidth (-10 dB, %)	GBWP (-10 dB)	CMOS Compatible
[9]	AlN/FeGaB	FBAR	BAW	2.55	-18	1.13%	0.02%$^{\#}$	3.17×10^{-6}	Yes
[47]	AlN/FeGaB	SMR	BAW	4.97	-25.1	3.58%	0%†	$0^{\dagger}$	Yes
[48]	$LiNbO_3$/FeGaB	SAW	SAW	0.43	-28	††	0.93%$^{\#}$	14.74×10^{-6}	No
[10]	AlScN/FeGaB	XBAR	BAW	0.268	-17.8	42.57%*	0%†	$0^{\dagger}$	Yes
[10]	AlScN/FeGaB	XBAR	BAW	0.973	-34.7	1.73%*	0.013%$^{\#}$	0.04×10^{-6}	Yes
[10]	AlScN/FeGaB	PFBAR	BAW	1.065	-32.9	1.85%*	0.01%$^{\#}$	0.05×10^{-6}	Yes
This work	AlScN/FeGaB	FBAR	BAW	2.62	-31.8	10%	1.28%	8.26×10^{-6}	Yes
This work	AlScN/FeCoSiB	FBAR	BAW	3.08	-29.7	10.7%	1.27%	13.83×10^{-6}	Yes

-10 dB fractional bandwidth estimated from figures and/or from provided MBVD fitting.
† The return loss is lower than 10 dB, thus not allowing us to quantify the -10 dB fractional bandwidth and therefore the GBWP (%).
†† k_t^2 and MBVD parameters not provided.
⋆ k_t^2 computed from provided MBVD parameters.

The extracted S_{21} parameters and realized gain values are reported in Figure 14 for the FeGaB-based BAW ME antenna and in Figure 15 for the FeCoSiB-based antenna, and are compared to their unreleased counterparts. We measure a maximum gain of -31.8 dB for the FeGaB-based device and -29.7 dB for the FeCoSiB-based device. As expected, a boost in total gain compared to the unreleased devices is visible around the minimum of the S_{11} values for both antennas, which by design choice corresponds to the f_p of both devices (see Figure 14). In this regard, the maximum gain levels we extracted for both antennas are in agreement with our FEM simulations shown in Figure 8. Also, as evident from Figure 14a and Figure 15a, the unreleased devices show no visible peak in the S_{21} parameter in the vicinity of the parallel resonance frequency of the BAW antennas. This is expected as the edges of the FBAR are not free to vibrate and therefore prevent the excitation of the TE mode. We note, however, that the gain vs frequency trends far from f_p (see Figures 14b and 15b) do not match the results obtained with our FEM simulation framework, which predicts a much steeper decrease in gain (see Figure 8). We attribute this discrepancy primarily to stray radiation and multipath interference from unshielded scatterers and from the GSG probes [49–51]. To support this claim, we run an additional experiment where we took two released antennas identical to those characterized in Figures 14b and 15b. Then, by using DC probes, we broke the FBAR structure for both antennas and replicate the exact measurements we have run for all configurations described in Figure 14b and Figure 15b. The broken device effectively behaves as an open circuit, without including any of the radiation contribution that we examined in our FEM simulation framework. Therefore, it can be considered a reliable indicator of the minimum S_{21} floor that can be measured with our setup. As evident from Figure 16, the S_{21} we measured for the broken devices match closely the S_{21} measured for the unreleased devices, proving that the out-of-resonance gain characteristics of the reported released antennas are indeed not determined by the FBAR structure.

Finally, we compare our work with previously reported ME antennas in Table **??**. Both our antennas exhibit k_t^2 values equal or higher than 10%, marking a significant improvement over most of the previously reported post-CMOS-compatible BAW ME antennas [9,10]. This enhanced coupling translates into an increase of approximately one order of magnitude in the -10 dB S_{11} bandwidth of our BAW ME antennas over previous AlN and AlScN-based counterparts. Specifically, this work shows -10 dB fractional bandwidths of 1.28% and 1.27% for FeGaB and FeCoSiB, which are the highest reported for ME antennas to date, and a higher -10 dB Gain Bandwidth product (GBWP).

4. Conclusions

In this work, we report on the design, modeling, and experimental characterization of the first two AlScN ME antennas with a Sc-doping concentration of 30% and operating above 1.1 GHz, employing FeGaB and FeCoSiB as magnetostrictive thin films. We describe a comprehensive modeling framework to quantify the power radiated not only by magnetoelastic coupling, but also from secondary sources, namely the electric dipole moment in the piezoelectric layer and the currents in the probing pads, both of which have been hypothesized to play a role in the operation of ME antennas. Our analysis establishes that magnetoelastic coupling is the dominant radiation mechanism, exceeding all other sources by several orders of magnitude.

We also provide design guidelines to maximize the radiated power and return loss when interfacing the antenna with a 50 Ω source. We determine that matching the antenna to 50 Ω at its anti-resonance frequency allows to design it with a larger active area, ultimately leading to improved radiation performance. Having established that, we analyze the role of k_t^2 on gain and -10 dB fractional bandwidth, showing that, when the peak return loss is kept constant by increasing the device area, the gain increases proportionally to $\left(k_t^2\right)^2$, with the -10 dB fractional bandwidth being approximately constant. Conversely, for a given device area, the -10 dB fractional bandwidth monotonically increases with k_t^2, provided that the return loss stays sufficiently high.

We conclude with the experimental characterization of the fabricated antennas, achieving realized gains of -31.8 dB and -29.7 dB at 2.62 GHz and 3.08 GHz for the FeGaB and FeCoSiB-based devices, respectively, and -10 dB fractional bandwidths of 1.28% and 1.27%. The latter, in particular, are the highest ones reported for ME antennas to date. Our findings provide a rigorous foundation for the continued development of AlScN BAW ME antennas, as their compatibility with post-CMOS fabrication processes makes them strong candidates for the development of next-generation chip-scale wireless sensing and communication systems.

Funding: This research was supported by National Science Foundation (NSF) under award No. 2414743.

Acknowledgments: The authors thank Matthew Moneck and Bennet Clark (Carnegie Mellon University, Pittsburgh, PA, USA), for their valuable assistance during the fabrication process. We also acknowledge Prof. Srinivas Tadigadapa, Chichen Huang and Shengli Zhang at Northeastern University (Boston, MA, USA) for their assistance with the material characterization.

Conflicts of Interest: The authors declare no conflicts of interest.

References

1. Liu, Y.; Cai, Y.; Zhang, Y.; Tovstopyat, A.; Liu, S.; Sun, C. Materials, design, and characteristics of bulk acoustic wave resonator: A review. *Micromachines* **2020**, *11*, 630.
2. Zhao, X.; Colombo, L.; Cassella, C. Aluminum nitride two-dimensional-resonant-rods. *Applied Physics Letters* **2020**, *116*, 143504. https://doi.org/10.1063/5.0005203.
3. Cassella, C.; Segovia-Fernandez, J. High k_t^2 Exceeding 6.4% Through Metal Frames in Aluminum Nitride 2-D Mode Resonators. *IEEE Transactions on Ultrasonics, Ferroelectrics, and Frequency Control* **2019**, *66*, 958–964. https://doi.org/10.1109/TUFFC.2019.2903011.
4. Hagelauer, A.; Ruby, R.; Inoue, S.; Plessky, V.; Hashimoto, K.Y.; Nakagawa, R.; Verdu, J.; de Paco, P.; Mortazawi, A.; Piazza, G.; et al. From microwave acoustic filters to millimeter-wave operation and new applications. *IEEE Journal of Microwaves* **2022**, *3*, 484–508.
5. Kalia, S.; Finocchiaro, S.; Dinc, T.; Bahr, B.; Raghunathan, A.; Schuppener, G.; Akhtar, S.; Fritz, T.; Haroun, B.S.; Cook, B.; et al. A sub-100 fs RMS jitter 20 GHz fractional-N analog PLL with a BAW resonator based on-chip 2.5 GHz reference. *IEEE Journal of Solid-State Circuits* **2022**, *57*, 1372–1384.

6. Daruwalla, A.; Wen, H.; Gong, M.; Ayazi, F. High-G and high-bandwidth bulk acoustic wave (BAW) accelerometers using a metal-less AlN-HARPSS process with 95 nm gaps. *IEEE Sensors Letters* **2020**, *4*, 1–4.
7. Chiu, K.H.; Chen, H.R.; Huang, S.R.S. High-performance film bulk acoustic wave pressure and temperature sensors. *Japanese journal of applied physics* **2007**, *46*, 1392.
8. Pisani, M.B.; Ren, K.; Kao, P.; Tadigadapa, S. Application of micromachined Y-cut-Quartz bulk acoustic wave resonator for infrared sensing. *Journal of Microelectromechanical Systems* **2011**, *20*, 288–296.
9. Nan, T.; Lin, H.; Gao, Y.; Matyushov, A.; Yu, G.; Chen, H.; Sun, N.; Wei, S.; Wang, Z.; Li, M.; et al. Acoustically actuated ultra-compact NEMS magnetoelectric antennas. *Nature communications* **2017**, *8*, 296.
10. Fu, Y.; Hu, R.; Li, J.; Li, D.; Song, Y.; Fang, B.; Lin, W.; Zeng, Z.; Zhu, X. XBAR-structured magnetoelectric antenna with magnetostrictive interdigital transducers. *IEEE Electron Device Letters* **2025**.
11. Liu, J.; Zhang, C.; Li, K.; Ji, Y.; Ma, S.; Zhang, P.; Liang, X.; Gao, H.; Guo, J.; Ren, T.; et al. Acoustically Mediated Piezoelectric Antennas with Asymmetric Excitation Using Acoustic and Electromagnetic Co-simulation. *IEEE Transactions on Antennas and Propagation* **2025**.
12. Cheema, H.M.; Shamim, A. The last barrier: on-chip antennas. *IEEE Microwave Magazine* **2013**, *14*, 79–91.
13. Quaresima, S.; Giribaldi, G.; Petrov, V.; Davaji, B.; Jornet, J.M.; Colombo, L.; Rinaldi, M.; Cassella, C. On-chip mmWave Antennas on a Piezoelectric ScAlN-Si Platform for 6G-grade Internet of Things. In Proceedings of the 2024 IEEE International Symposium on Antennas and Propagation and INC/USNC-URSI Radio Science Meeting (AP-S/INC-USNC-URSI). IEEE, 2024, pp. 2171–2172.
14. Kong, S.; Shum, K.M.; Yang, C.; Gao, L.; Chan, C.H. Wide impedance-bandwidth and gain-bandwidth terahertz on-chip antenna with chip-integrated dielectric resonator. *IEEE Transactions on Antennas and Propagation* **2021**, *69*, 4269–4278.
15. Ji, Y.; Zhang, C.; Gu, H.; Zhang, P.; Liu, J.; Yang, F.; Nan, T. Evaluation of electromagnetic radiation from ultra-compact magnetoelectric antennas. In Proceedings of the 2024 IEEE International Symposium on Antennas and Propagation and INC/USNC-URSI Radio Science Meeting (AP-S/INC-USNC-URSI). IEEE, 2024, pp. 2235–2236.
16. Xu, R.F.; Ippet-Letembet, L.C.; Tiwari, S.; Yao, Z.J.; Huang, S.M.; Candler, R.N.; Chen, S.Y. Experimental validation of multiferroic antennas in GHz frequency range. *Applied Physics Letters* **2023**, *123*.
17. Cai, X.; Wan, R.; Ding, R.; Wu, J.; Li, J.; Zhang, K.; Lu, J.; Hazarika, D.; Xu, L.; Ni, J.; et al. Multi-mode piezoelectric radiation-based microantennas and miniaturized wireless sensing unit driven by bulk acoustic waves. *Nature Communications* **2026**.
18. Ruby, R.C.; Bradley, P.; Oshmyansky, Y.; Chien, A.; Larson, J.D. Thin film bulk wave acoustic resonators (FBAR) for wireless applications. In Proceedings of the 2001 IEEE Ultrasonics Symposium. Proceedings. An International Symposium (Cat. No. 01CH37263). IEEE, 2001, Vol. 1, pp. 813–821.
19. Dong, C.; Li, M.; Liang, X.; Chen, H.; Zhou, H.; Wang, X.; Gao, Y.; McConney, M.E.; Jones, J.G.; Brown, G.J.; et al. Characterization of magnetomechanical properties in FeGaB thin films. *Applied Physics Letters* **2018**, *113*.
20. Kurz, N.; Ding, A.; Urban, D.F.; Lu, Y.; Kirste, L.; Feil, N.M.; Žukauskaitė, A.; Ambacher, O. Experimental determination of the electro-acoustic properties of thin film AlScN using surface acoustic wave resonators. *Journal of Applied Physics* **2019**, *126*.
21. Ambacher, O.; Christian, B.; Feil, N.; Urban, D.; Elsässer, C.; Prescher, M.; Kirste, L. Wurtzite ScAlN, InAlN, and GaAlN crystals, a comparison of structural, elastic, dielectric, and piezoelectric properties. *Journal of Applied Physics* **2021**, *130*.
22. Larson, J.D.; Bradley, P.D.; Wartenberg, S.; Ruby, R.C. Modified Butterworth-Van Dyke circuit for FBAR resonators and automated measurement system. In Proceedings of the 2000 IEEE ultrasonics symposium. proceedings. an international symposium (Cat. No. 00CH37121). IEEE, 2000, Vol. 1, pp. 863–868.
23. Chen, G.; Cassella, C.; Qian, Z.; Hummel, G.E.; Rinaldi, M. Lithographically defined aluminum nitride cross-sectional Lamé mode resonators. *Journal of Micromechanics and Microengineering* **2017**, *27*, 034003. https://doi.org/10.1088/1361-6439/aa58c1.
24. Ruby, R. 11E-2 review and comparison of bulk acoustic wave FBAR, SMR technology. In Proceedings of the 2007 IEEE Ultrasonics Symposium Proceedings. IEEE, 2007, pp. 1029–1040.
25. Zhao, X.; Cassella, C. On the Coupling Coefficient of $\mathrm{Sc}_y\mathrm{Al}_{1-y}$N-Based Piezoelectric Acoustic Resonators. In Proceedings of the 2019 Joint Conference of the IEEE International Frequency Control Symposium and European Frequency and Time Forum (EFTF/IFCS). IEEE, 2019, pp. 1–4. https://doi.org/10.1109/IFCS.2019.8856086.
26. Hansen, R.C. *Electrically small, superdirective, and superconducting antennas*; John Wiley & Sons, 2006.

27. Yang, J. *An introduction to the theory of piezoelectricity*; Springer, 2005.
28. Liu, X.; Zheng, X. A nonlinear constitutive model for magnetostrictive materials. *Acta Mechanica Sinica* **2005**, *21*, 278–285.
29. Cullity, B.D.; Graham, C.D. *Introduction to magnetic materials*; John Wiley & Sons, 2011.
30. Hashimoto, K.y. BAW piezoelectric resonators. In *Piezoelectric MEMS Resonators*; Springer, 2017; pp. 203–220.
31. Pozar, D.M. *Microwave engineering*; John wiley & sons, 2011.
32. Balanis, C.A. *Antenna theory: analysis and design*; John wiley & sons, 2016.
33. Becker, R.; Döring, W. *Ferromagnetismus*; Springer-Verlag, 2013.
34. Liang, X.; Dong, C.; Chen, H.; Wang, J.; Wei, Y.; Zaeimbashi, M.; He, Y.; Matyushov, A.; Sun, C.; Sun, N. A review of thin-film magnetoelastic materials for magnetoelectric applications. *Sensors* **2020**, *20*, 1532.
35. Caro, M.A.; Zhang, S.; Riekkinen, T.; Ylilammi, M.; Moram, M.A.; Lopez-Acevedo, O.; Molarius, J.; Laurila, T. Piezoelectric coefficients and spontaneous polarization of ScAlN. *Journal of Physics: Condensed Matter* **2015**, *27*, 245901.
36. Jackson, J.D.; Fox, R.F. Classical electrodynamics, 1999.
37. Yao, Z.; Wang, Y.E.; Keller, S.; Carman, G.P. Bulk Acoustic Wave-Mediated Multiferroic Antennas: Architecture and Performance Bound. *IEEE Transactions on Antennas and Propagation* **2015**, *63*, 3335–3344. https://doi.org/10.1109/TAP.2015.2431723.
38. Orfanidis, S.J. Electromagnetic waves and antennas **2002**.
39. Campbell, C.; Weber, R. Calculation of radiated electromagnetic power from bulk acoustic wave resonators. In Proceedings of the 1993 IEEE International Frequency Control Symposium. IEEE, 1993, pp. 472–475.
40. Hassanien, A.E.; Breen, M.; Li, M.H.; Gong, S. A theoretical study of acoustically driven antennas. *Journal of Applied Physics* **2020**, *127*.
41. Kang, J.M. Piezoelectric MEMS resonator characterization and filter design. PhD thesis, Massachusetts Institute of Technology, 2004.
42. Giribaldi, G.; Colombo, L.; Bersano, F.; Cassella, C.; Rinaldi, M. Investigation on the Impact of Scandium-doping on the kt2 of ScxAl1-xN Cross-sectional Lamé Mode Resonators. In Proceedings of the 2020 IEEE International Ultrasonics Symposium (IUS), 2020, pp. 1–4. https://doi.org/10.1109/IUS46767.2020.9251829.
43. Kaya, O.; Colombo, L.; Simeoni, P.; Davaji, B.; Rinaldi, M.; Cassella, C. A Radiofrequency Threshold Temperature Sensor Using a Hf 0.5 Zr 0.5 O 2 Device and a Microacoustic Piezoelectric Resonant Sensor. *Journal of Microelectromechanical Systems* **2024**, *33*, 151–162.
44. Zhao, X.; Kaya, O.; Pirro, M.; Assylbekova, M.; Colombo, L.; Simeoni, P.; Cassella, C. A 5.3 GHz Al0.76Sc0.24N Two-Dimensional Resonant Rods Resonator With a kt2 of 23.9 *Journal of Microelectromechanical Systems* **2022**, *31*, 561–570. https://doi.org/10.1109/JMEMS.2022.3178978.
45. Ren, W.; Li, J.; Chen, S.; Wang, G.; Zhu, P.; Chen, J. Eddy current suppression and soft magnetism enhancement in FeGaB-based magnetic composites with alumina lamination. *Journal of Magnetism and Magnetic Materials* **2023**, *574*, 170714.
46. Luo, B.; Liang, X.; Chen, H.; Sun, N.; Lin, H.; Sun, N.X. Gain enhancement and ground plane immunity of mechanically driven thin-film bulk acoustic resonator magnetoelectric antenna arrays. *Advanced Functional Materials* **2024**, *34*, 2403244.
47. Ma, M.; Chen, C.; Xu, H.; Liu, P.; Xiao, B.; Liang, S.; Fu, S.; Song, C.; Pan, F. High-frequency magnetoelectric antenna by acoustic excitation for 5G communication. *IEEE Antennas and Wireless Propagation Letters* **2024**, *23*, 1518–1522.
48. Zhang, C.; Ji, Y.; Gu, H.; Zhang, P.; Liu, J.; Liang, X.; Yang, F.; Ren, T.; Nan, T. Surface acoustic wave actuated MEMS magnetoelectric antenna. *IEEE Electron Device Letters* **2024**, *45*, 2009–2012.
49. Liu, J.; Zhang, C.; Li, K.; Ji, Y.; Zhang, P.; Ju, D.; Lu, Y.; Liang, X.; Ren, T.; Yang, F.; et al. Accurate Radiation Evaluation of Electrically Small On-Chip Acoustically Actuated Antennas. *IEEE Antennas and Wireless Propagation Letters* **2025**, *25*, 423–427.
50. Zheng, Z.; Zhang, Y.P. A study on the radiation characteristics of microelectronic probes. *IEEE Open Journal of Antennas and Propagation* **2021**, *3*, 4–11.
51. Huitema, L.; Delaveaud, C.; d'Errico, R. Impedance and radiation measurement methodology for ultra miniature antennas. *IEEE Transactions on Antennas and Propagation* **2014**, *62*, 3463–3473.

doi:10.20944/preprints202605.0722.v1